Tectonics

RESEARCH ARTICLE
10.1029/2020TC006305

An Exhumation Pulse From the Nascent Franciscan Subduction Zone (California, USA)

Daniel Rutte[1,2,3], Joshua Garber[4], Andrew Kylander-Clark[5], and Paul R. Renne[2,3]

[1]Institut für Geowissenschaften, University of Bonn, Bonn, Germany, [2]Berkeley Geochronology Center, [3]Departmant of Earth and Planetary Sciences, University of California, Berkeley, CA, USA, [4]Department of Geosciences, The Pennsylvania State University, [5]Department of Earth Science, University of California, Santa Barbara, CA, USA

Key Points:
- Franciscan high-grade blocks experienced fast and uniform exhumation from the eclogite facies into the blueschist facies
- Eclogite/amphibolite exhumation was a discontinuous one-time event correlated with Cordilleran wide geodynamics
- Sierra foothills blueschist metamorphism is temporally unrelated to Franciscan subduction initiation

Supporting Information:
- Supporting Information S1

Correspondence to:
D. Rutte,
d.rutte@gmx.de

Citation:
Rutte, D., Garber, J., Kylander-Clark, A., & Renne, P. R. (2020). An exhumation pulse from the nascent Franciscan subduction zone (California, USA). *Tectonics*, *39*, e2020TC006305. https://doi.org/10.1029/2020TC006305

Received 20 MAY 2020
Accepted 10 AUG 2020
Accepted article online 31 AUG 2020

Abstract We investigated a suite of metabasite blocks from serpentinite matrix and shale matrix mélanges of the California Coast Ranges. Our new data set consists of $^{40}Ar/^{39}Ar$ dates of amphibole and phengite and U-Pb dates of metamorphic zircon. Combined with published geochronology, including prograde Lu-Hf garnet ages from the same blocks, we can reconstruct the timing and time scales of prograde and retrograde metamorphism of individual blocks. In particular we find that exhumation from amphibole-eclogite facies conditions occurred as a single episode at 165–157 Ma, with an apparent southward younging trend. The rate and timing of exhumation were initially uniform (when comparing individual blocks) and fast (with cooling rates up to ~140°C/Ma). In the cooler and shallower blueschist facies, exhumation slowed and became less uniform among blocks. Considering the subduction zone system, the high-grade exhumation temporally correlates with a magmatic arc pulse (Sierra Nevada) and the termination of forearc spreading (Coast Range Ophiolite). Our findings suggest that a geodynamic one-time event led to exhumation of amphibole-eclogite facies rocks. We propose that interaction of the Franciscan subduction zone with a spreading ridge led to extraction of the forearc mantle wedge from its position between forearc crust and subducting crust. The extraction led to fast and uniform exhumation of subducted rocks into the blueschist facies. We also show that the Franciscan subduction zone did not undergo significant cooling over time and that its initiation was not coeval with blueschist-facies metamorphism of the Red Ant schist of the Sierra Nevada foothills.

Plain Language Summary A subduction zone is where oceanic crust of one tectonic plate dives under the crust of another plate. These zones are important drivers of the movement of the continental plates. Special rocks—blueschists and eclogites—form in subduction zones at high pressure and relatively low temperature. The Franciscan Complex forms most of the geology of western California. It consists of rocks that dived into a subduction zone and returned back to the surface. We investigated the history of some of these rocks by determining the age and conditions of their movement. We find that the rocks that subducted to depths of up to 80 km all came up at the same time around 160 million years before present. This suggests that a specific tectonic event occurred at that time; other regional data show that the effects of this event were felt elsewhere along the paleo-Pacific margin. We also investigate rocks in the Sierra Nevada foothills that other researchers suggested to have formed at about the same time and found that they are not correlated.

1. Introduction

Metamorphic histories of subducted and exhumed rocks reflect a range of thermomechanical processes operative in subduction zones (Coleman & Lanphere, 1971; Ernst, 1973). Data from these rocks provide quantitative constraints on volatile recycling (e.g., Hacker, 2008; Hacker et al., 2003), plate-interface rheology (e.g., Agard et al., 2018, and references therein), and chemical-physical responses to changes in subduction-zone boundary conditions (e.g., Bebout, 2007). Quantifying these processes relies on a robust knowledge of subduction-zone thermal structure and its global variation (Syracuse et al., 2010), but subduction zone pressure-temperature (*P-T*) conditions determined on exhumed rocks exhibit a thermal structure that may not match results obtained from numerical modeling (Penniston-Dorland et al., 2015). Such discrepancies suggest that modeling approaches and/or rock observations are incomplete, for example, either by model (Kohn et al., 2018) or rock bias (van Keken et al., 2018). One way to assess the bias inherent to the subducted rock record is to examine variations in *P-T-t* histories

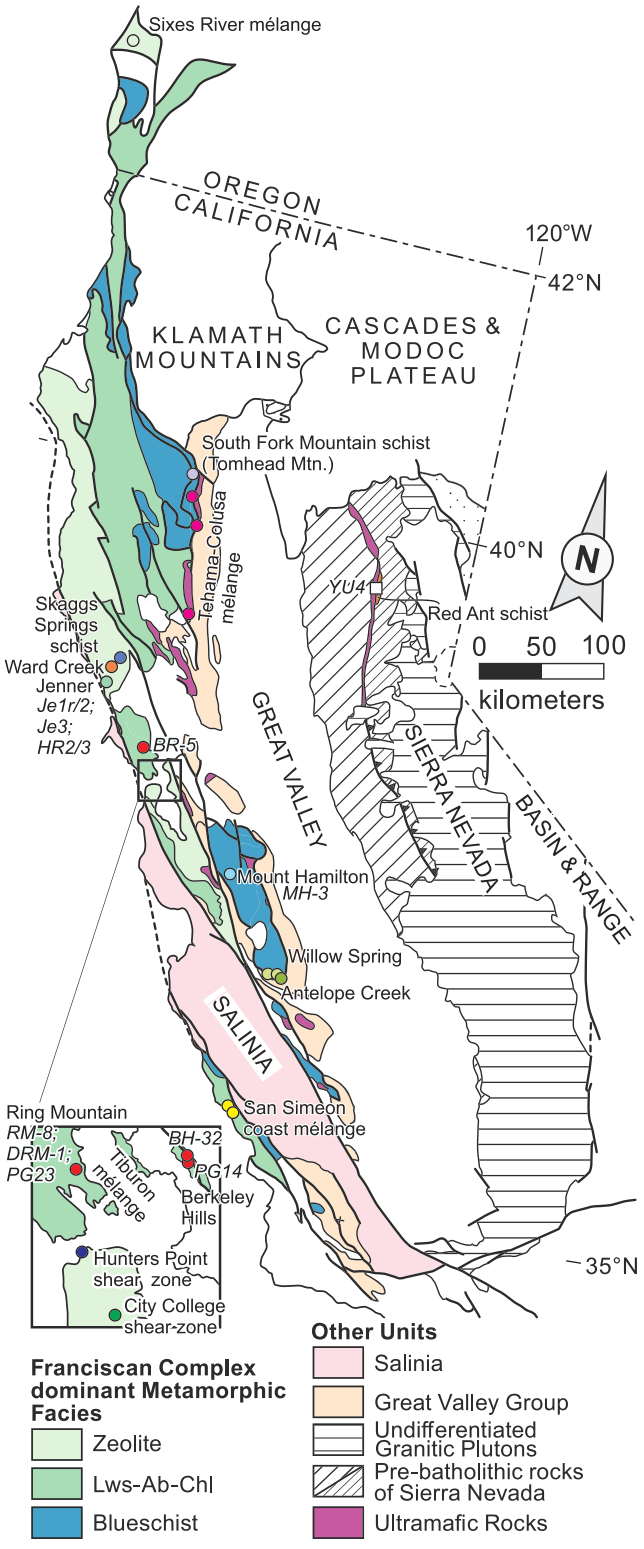

Figure 1. Tectonic and metamorphic overview map of northern and central California. Samples discussed in detail in the text are labeled with italicized letter. Modified from Mulcahy et al. (2018).

within individual subduction complexes. These data suggest that most subduction zones record synchronous, punctuated exhumation, indicating that exhumation is likely driven by changes in boundary conditions (Agard et al., 2009) and may not represent a thermal steady state. On the other hand, some studies have determined lengthy residence times for individual blocks prior to exhumation (Tamblyn et al., 2019), such that comprehensive *P-T-t* data from multiple blocks may expose the time-resolved thermal structure, or metamorphic field gradient, of an individual subduction zone.

The Franciscan Complex is regarded as the classic example of a subduction-accretion complex, with a history of continuous subduction exceeding 150 Ma (Hamilton, 1969; Mulcahy et al., 2018; Wakabayashi, 2015). The oldest metamorphic ages presumably date subduction initiation, initially thought to be ~150 Ma (Coleman & Lanphere, 1971), since revised to ~169 Ma (Anczkiewicz et al., 2004), and recently determined to be ~180 Ma (Mulcahy et al., 2018). These old ages stem solely from high-grade, amphibole-eclogite facies blocks in lower-grade, shale or serpentinite matrices that make up <1% of the Franciscan Complex but are the only material record of subduction zone metamorphism from ~180 to 132 Ma; at ~123 Ma there was a significant change in both the volume and type of accreted material (Figure 2a; Dumitru et al., 2010; Wakabayashi & Dumitru, 2007) (Dumitru et al., 2010). There is a wide range of hornblende and phengite K-Ar and $^{40}Ar/^{39}Ar$ dates (see Wakabayashi & Dumitru, 2007, for a review) that may indicate continuous exhumation of amphibolites and eclogites over a ~20–30 Ma period. However, despite decades of research on the Franciscan Complex, coupled geochronology (U-Pb zircon, Lu-Hf garnet) and thermochronology ($^{40}Ar/^{39}Ar$ hornblende, $^{40}Ar/^{39}Ar$ phengite) have rarely been performed on the same blocks—such that published radiometric ages are often sourced from different blocks with potentially distinct metamorphic histories.

In this study, we performed $^{40}Ar/^{39}Ar$ hornblende, $^{40}Ar/^{39}Ar$ phengite, and U-Pb zircon geochronology on exhumed blocks from the Franciscan Complex, to assess (i) how individual blocks recorded the metamorphic history of the Franciscan subduction zone, including the long-term subduction geotherm, and (ii) when and how changes occurred in the Franciscan thermal structure. These questions are answered with targeted analyses on high-grade eclogite, amphibolite, and blueschist blocks distributed geographically throughout the Franciscan Complex (Figure 1). Many of these blocks have been previously dated by the Lu-Hf garnet method, providing essential prograde-to-peak metamorphic context. To further clarify the regional tectonic setting, we analyzed an additional rock from the Western Sierra Metamorphic Belt (Red Ant schist; Schweickert et al., 1980) that has been previously posited to temporally correlate with Franciscan subduction initiation (Ernst, 2011). Our results reveal that exhumation of high-pressure eclogites occurred almost synchronously along a significant length of the Franciscan margin, suggesting a coherent, orogeny-wide tectonic, or geodynamic trigger. Coupled with *P–T* data from the literature, we further show that the early Franciscan geotherm may have been characterized by heating along the plate interface, rather than the cooling inferred elsewhere (e.g., Anczkiewicz et al., 2004).

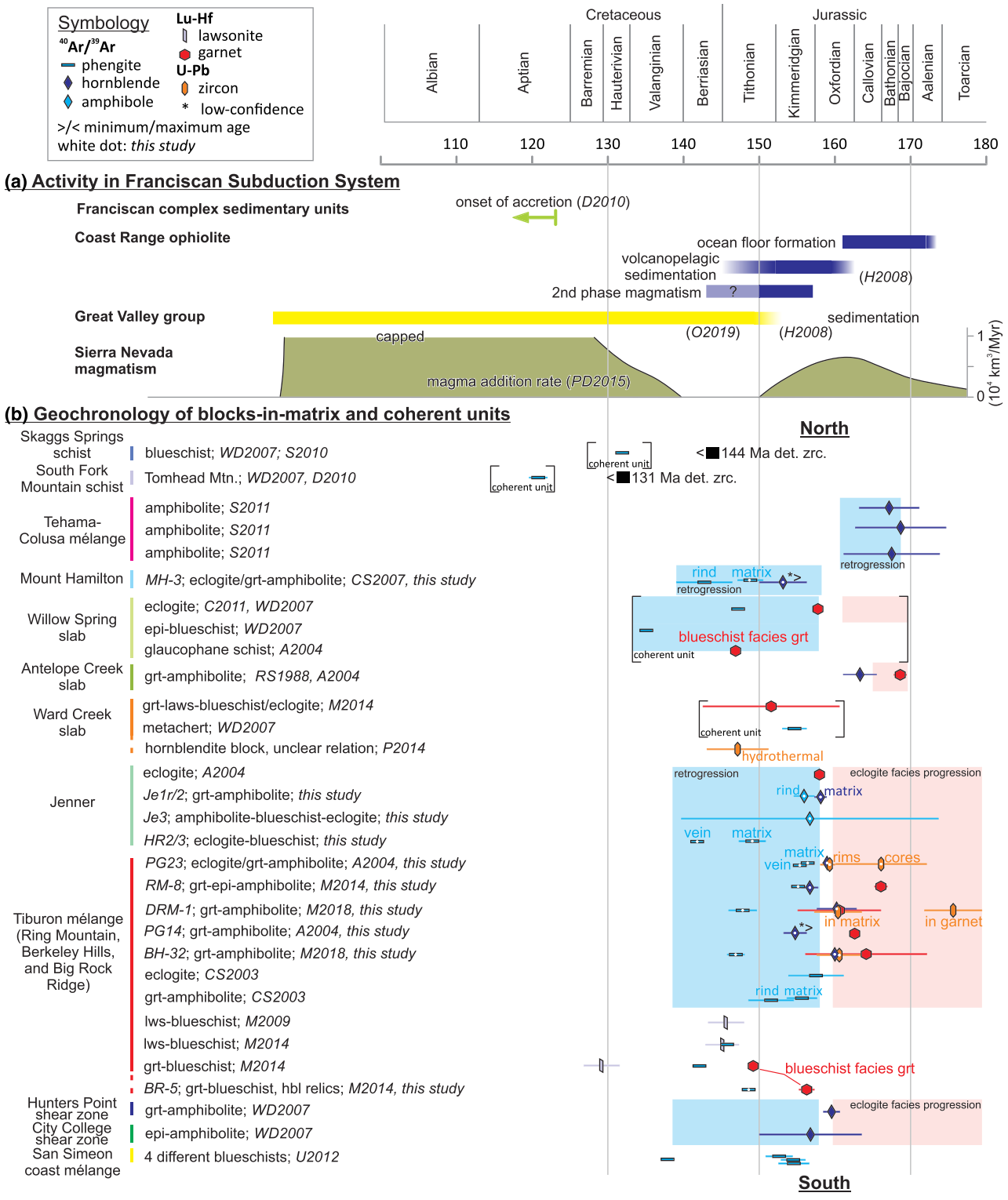

Figure 2. Chronology of events in the Franciscan subduction system. (a) Chronology of accretion of Franciscan Complex sedimentary units, Coast range ophiolite genesis, Great Valley group sedimentation, and Sierra Nevada magmatism. (b) Summary of geochronologic data for Franciscan high-grade bocks and coherent units. Investigated locales in the Franciscan Complex are color coded in conjunction with Figure 1. Localities are sorted from North to South based on their position prior to Cenozoic strike-slip motion (reconstruction of Wakabayashi, 1999). Abbreviations: A2004 (Anczkiewicz et al., 2004); CS2007 (Catlos & Sorensen, 2003); C2011 (Cooper et al., 2011); D2010 (Dumitru et al., 2010); H2008 (Hopson et al., 2008); M2009 (Mulcahy et al., 2009); M2014 (Mulcahy et al., 2014); M2018 (Mulcahy et al., 2018); O2019 (Orme & Surpless, 2019); P2014 (Page et al., 2014); PD2015 (Paterson & Ducea, 2015); RS1988 (Ross & Sharp, 1988); S2010 (Snow et al., 2010); S2011 (Shervais et al., 2011); U2012 (Ukar et al., 2012); WD2007 (Wakabayashi & Dumitru, 2007).

2. Geologic Setting: Franciscan Subduction System

The Franciscan subduction system comprises the Franciscan accretionary complex, the Sierra Nevada magmatic arc, the interjacent Coast Range Ophiolite, and Great Valley group forearc basin (Figure 1). The Franciscan Complex consists of mixed mafic, metasedimentary, and mantle material in various mélanges, coherent blocks, and thrust sheets along the length of coastal California. Though a full discussion is beyond the scope of this study, we briefly review components of the subduction system relevant to this paper. We also discuss a unit from the Western Sierra metamorphic belt (Red Ant schist) that was previously suggested to relate to the Franciscan subduction system and is dated in this study.

2.1. Franciscan Mélanges

Mélanges with shale, serpentinite, or mixed matrices enclosing lithologically variable blocks are an important component of the Franciscan Complex. These mélanges occur between coherent nonmélange units of different metamorphic grade, along imbrications of such units, and along the boundary with the Coast Range ophiolite (see Wakabayashi, 2011, for a review). Recent observations suggest that the mélanges accreted together with the nonmélange units and should be considered part of the nappes (Wakabayashi, 2015, 2017b). Two endmember mélange types occur in the Franciscan. The first includes block-in-matrix mélanges with all blocks having the same metamorphic grade as the matrix and lithologies of either or both flanking units. These are generally agreed on to be of tectonic origin, resulting from progressive deformation. The second class of block-in-matrix mélanges contain "exotic" blocks that differ in lithology and metamorphic grade from the flanking units and matrix, respectively. Their formation is disputed, and they are the focus of this study.

Blocks in these mélanges include metabasites (metagabbro, blueschist, eclogite, and garnet amphibolite) and metasedimentary rocks (cherts, sandstones, and sedimentary breccias) that show significant variance in proportions and metamorphic grade (Coleman & Lanphere, 1971; Wakabayashi, 2011). The Tehama-Colusa mélange along the contact of the Franciscan Complex and Coast Range ophiolite (CRO) additionally contains unmetamorphosed ophiolitic blocks, likely derived from the CRO (Figure 1; MacPherson et al., 2006; Shervais et al., 2011; Wakabayashi, 2015). Cloos (1982; see also Cloos & Shreve, 1988a, 1988b) ascribed a tectonic origin to Franciscan mélanges suggesting mixing of (exotic) high-grade blocks into low-grade shale matrix within a subduction channel. This model was expanded on by the numerical models of Gerya et al. (2002) that adopted serpentinite as the dominant matrix material. Other studies suggest that several shale- and serpentinite-matrix mélanges preserve sedimentary structures and thus reflect exhumation of material (including high-grade blocks) to the surface, followed by mass wasting transport and mixing, redeposition, then (re)subduction accompanied by strong shearing (e.g., Hitz & Wakabayashi, 2012; Platt, 2015; Wakabayashi, 2011, 2012, 2019). These accordingly suggest a sedimentary origin.

2.2. Franciscan High-Grade Metabasites

The largest coherent amphibole-eclogite grade units are kilometers in size (e.g., Willow Spring slab and Antelope Creek slab; Hermes, 1973; Wakabayashi & Dumitru, 2007), whereas the smallest investigated garnet-amphibolite block in this study (PG14) is approximately 40 cm in diameter. The large coherent high-grade units are differentiated from blocks by scale and by lacking a shale or serpentinite matrix surrounding them (Wakabayashi, 2015). No intermediate, felsic, or sedimentary bulk compositions are described within the larger coherent units, suggesting that their protoliths were never exposed to input of continental detritus. Absence of continental input is further supported by the lack of LREE-rich compositions in the high-grade units (Saha et al., 2005; Wakabayashi et al., 2010). Geochemical analyses of eclogites and garnet-amphibolite showed significant enrichments in immobile Th, Ba, and Pb relative to N-MORB and were interpreted to point to a nascent arc (suprasubduction) origin of the blocks (Saha et al., 2005; Wakabayashi et al., 2010). It should however be noted that based on differing assessment of chemical mobility during subduction zone metamorphism, the reliability of such interpretation is debated (Ghatak et al., 2012).

The *P-T* evolution of the high-grade blocks has been studied since the recognition of eclogite by Switzer (1945), and there has been general agreement on the observation of three parageneses of (i) taramitic/katophoritic/barroisitic amphibole + garnet, (ii) omphacite + garnet and (iii) glaucophane ± phengite ± lawsonite ± garnet (e.g., Mulcahy et al., 2018; Tsujimori et al., 2006;

Wakabayashi, 1990). However, there is a prevailing disagreement on the temporal order of the hornblende and omphacite bearing parageneses. For example, Krogh et al. (1994) and Wakabayashi (1990) interpreted hornblende inclusions in omphacite and garnet to indicate a counter-clockwise *P-T* path with an initial amphibolite-facies peak *T*, followed by a later, eclogite-facies peak *P* overprint at similar or lower temperature. In contrast, Mulcahy et al. (2018) observed inclusion of omphacite in hornblende and interpreted a clockwise *P-T* path, with initial high-pressure eclogite-facies metamorphism followed by a higher-temperature amphibolite overprint. Moreover, Tsujimori et al. (2006) worked on the same blocks as Wakabayashi (1990) and concluded a hairpin PT-path toward the amphibole-eclogite facies in which the prograde and retrograde path approximately overlie each other. Despite these disagreements, all above cited studies agree on a variably strong, late blueschist-facies overprint of the eclogite/amphibolite blocks.

Independently of their now-enclosing matrix, many of the eclogite/amphibolite blocks have peripheral or internal reaction zones composed of hydrous minerals, primarily actinolite, epidote, phengite, talc, and chlorite (Wakabayashi, 2019). These rinds have been classically interpreted to have formed at the outer contact of the block with serpentinite by mechanical mixing and metasomatic alteration hybridizing the block and matrix (Coleman & Lanphere, 1971; Penniston-Dorland et al., 2014). A revised interpretation is proposed by Wakabayashi (2017b, 2019) who points out that the internal reaction zones are very common and likely formed along imbricates of ultramafic schists. Also, peripheral rinds are typically found only along parts of the periphery of a block. Based on these observations they suggest that many or all of the peripheral rinds formed as internal selvages and came into their peripheral position only upon breakup of the blocks. The ubiquity of these features indicates that many, if not all, of the high-grade blocks were at some point either encased in an ultramafic (serpentinite) matrix or imbricated with ultramafic layers, even if they are now exposed within a shale matrix.

2.3. Coast Range Ophiolite

Twenty-two remnants of the CRO occur scattered over ~600 km along the California Coast Ranges (Bailey et al., 1970; Hopson et al., 2008). They encompass variably complete ophiolitic successions from upper mantle peridotite to volcanic and sedimentary cover, exposed in $\leq$3 km thick sections. Where contacts are exposed, these ophiolitic remnants have been tectonically juxtaposed with the structurally lower Franciscan Complex, whereas a sedimentary contact is preserved with the structurally higher Great Valley group (Bailey et al., 1970; Hopson et al., 2008). Based on crustal-scale seismic and gravity data, Constenius et al. (2000) estimate the overthrust length of CRO on the Franciscan Complex to be >60 km without any intervening forearc mantle.

A multiphase formation process for the CRO is well established (Figure 2a; Hopson et al., 2008; Shervais et al., 2004). The main phase of CRO crystallization is constrained with TIMS and LA-ICP-MS U-Pb dates of zircons ranging from 172.0 $\pm$ 4.0 to 161.13 $\pm$ 0.11 Ma; these zircons are separated from texturally late plagiogranites within gabbroic crust barren of zircon in eight of the remnants (Hopson et al., 2008). This magmatic phase is ascribed to a supra subduction origin based on geochemical data by Metcalf and Shervais (2008) and Shervais et al. (2005), while Hopson et al. (2008) ascribed it to a "typical" spreading center and related off-axis magmatism based on paleomagnetic and biostratigraphic arguments. A full consideration of these two interpretations is beyond the scope of this study, but the recent recognition of Franciscan subduction initiation by ~176 Ma (Mulcahy et al., 2018)—that is, prior to the formation of the CRO—favors a supra-subduction origin for the CRO.

The Middle Jurassic ophiolite is disconformably overlain by an Oxfordian to upper Tithonian (~163.5–145.0 Ma) volcanopelagic succession of radiolarian ooze and waterlain tuff, as well as locally coarser andesitic to rhyolitic volcaniclastic marine sediments (Figure 2a). A later magmatic phase resulted in the emplacement of basaltic to silicic sheets crosscutting the CRO; these are as young as 150 $\pm$ 2 Ma ($^{40}Ar/^{39}Ar$ hornblende; Evarts et al., 1992). Young basaltic magmatism has a distinct MORB-like signature and was interpreted to indicate subduction of a spreading ridge beneath the CRO (Shervais et al., 2004). Due to a lack of documentation of many geochronologic ages that are published only in conference abstracts, the correlation between ages and geochemical phase classifications remains mostly tentative (Shervais et al., 2004) and is partly driven by different interpretations regarding the tectonic setting of ophiolite formation (e.g., Hopson et al., 2008; Shervais et al., 2005). Additionally, several $^{40}Ar/^{39}Ar$ dates (e.g., Evarts et al., 1992)

cannot be recalculated with a recent $^{40}Ar/^{39}Ar$ age standard recalibration because the data lack sufficient detail, although the new calibration will likely make these dates older by only a few Ma.

2.4. Great Valley Group

The Great Valley group was deposited atop the CRO. Where CRO remnants are absent, its contact with the structurally deeper Franciscan Complex is a fault contact (Constenius et al., 2000; Ernst, 1970). The Great Valley group consists of mudstone with turbiditic silt- and sandstone and submarine fanglomerate at the base (basin-plain deposits) that grade upward into a classical forearc basin succession (Ingersoll et al., 1978). The basal age of sedimentation is a matter of recent debate: Biostratigraphic constraints based on *Buchia* zones indicate sedimentation in the late Kimmeridgian (~155 Ma) in northern California to late Tithonian (~145 Ma) in central California (Figure 2a; Hopson et al., 2008, and references therein). However, detrital zircons with Cretaceous U-Pb ages in many of the near-base sandstones previously assigned to the Jurassic in Northern California contradict this assignment (Figure 2a; Orme & Surpless, 2019; Surpless et al., 2006). Calculated maximum deposition ages range 153–135 Ma and imply a temporal gap between CRO formation and the beginning of Great Valley group deposition of up to 15–23 Ma in four studied sites (Orme & Surpless, 2019).

2.5. Sierra Nevada Batholith

The Sierra Nevada batholiths (Figure 1) consist of Mesozoic granitoids intruding Proterozoic to Mesozoic volcano-sedimentary units. Compilation of U-Pb ages indicates three distinct phases of plutonism in the Late Triassic (257–185 Ma, peak at ~221 Ma), in the Middle Jurassic (185–143 Ma, peak at ~158 Ma), and in the Cretaceous (127–81 Ma, peak at ~99 Ma) with the last pulse being the most voluminous (Figure 2a; Paterson & Ducea, 2015).

2.6. Red Ant Schist

A major tectonic suture zone east of the Franciscan is traced by the Feather River ultramafic belt, a N-S trending string of blueschist-facies ultramafic, metabasaltic, and metasedimentary units (Figure 1; various classification scheme of Sierra Nevada foothills terranes are reviewed by Taylor et al., 2010). Among the best investigated higher-grade units along this suture is the Red Ant schist, a coherent unit of blueschist-facies metasedimentary and metabasaltic rocks cropping out along the Melones shear zone together with serpentinite (Figure 1; Schweickert et al., 1980). Phengite from the Red Ant schist yielded K/Ar dates of 157–190 Ma and were interpreted as a minimum age of blueschist-facies metamorphism (Schweickert et al., 1980). These ages suggested that the suture zone may be temporally correlated with early Franciscan subduction (e.g., Ernst, 2011). The Red Ant schist is also lithologically similar to the Stuart Fork blueschists in the Klamath Mountains (Hacker & Goodge, 1990), from which phengites were dated at ~214–223 Ma (K/Ar; Hotz et al., 1977). Hacker and Goodge (1990) and Hacker (1993) pointed out that the K/Ar ages from the Red Ant schist (in contrast to the Stuart Fork blueschists) may be influenced by a late, greenschist-facies overprint.

2.7. Other Regional Data

Several events and changes in the Mid- to Late Jurassic evolution of the north Pacific region are approximately coeval with the investigated processes in the Franciscan at 180–150 Ma. In the western Sierra Nevada, metamorphic belt forearc sedimentation occurred until 174 Ma, followed by deformation and metamorphism until 165 Ma (Hacker, 1993). North of the Franciscan Complex, in the Klamath Mountains, the crust of the Josephine ophiolite formed by ~160 Ma (U-Pb zircon in plagiogranite) and experienced a second phase of magmatism at 154–149 Ma (U-Pb zircon in cross-cutting silicic intrusions; Saleeby et al., 1982). The Sixes River mélange of the Franciscan Complex of Oregon hosts block-in-matrix mélanges with blueschist, amphibolite, and eclogite blocks (Blake et al., 1985) that appear similar to the here studied units and may be their northward prolongation; few available K/Ar data are consistent with K/Ar data from the Franciscan mélanges of California (Coleman & Lanphere, 1971). The Easton metamorphic suite in the northwest Cascades documents metamorphic sole formation in an initiating subduction zone between >167 and 164 (Cordova et al., 2019). In the Canadian Cordillera, marine basins of the Slide mountain terrane were deformed during the accretion of the Quesnellia island arc to the continental margin at 187–174 Ma (Murphy et al., 1995). The Talkeetna arc in southern Alaska formed at 174–158 Ma, while in northern Alaska the beginning closure of the oceanic Angayucham basin is dated by obduction of the Brooks range

ophiolite at 169–163 Ma (Wirth et al., 1993; $^{40}Ar/^{39}Ar$ hornblende, not recalculated because age standard is unknown).

3. Methods

3.1. Sampling

By design of the study, most of the investigated blocks have been previously described and analyzed with various methods. Except for sample BR-5 that was made available by Sean Mulcahy, all blocks were resampled without knowledge of the exact previous sampling location(s) on the block. Thus, given sample names designate identical blocks, not the same individual samples.

3.2. $^{40}Ar/^{39}Ar$ Analysis of Phengite and Amphibole

Samples were crushed, sieved, and ultrasonicated in deionized water. Phengite and amphibole (mostly hornblende *sensu lato*, cf. Table 1) were concentrated using magnetic separation and a dry shaking table. Pure mineral separates were handpicked from the largest possible sieve fraction.

The separates were loaded in wells in Al discs bracketed with Fish Canyon sanidine (FCs) as a geological age standard (28.294 ± 0.036 Ma; Renne et al., 2010, 2011). Neutron irradiations were carried out in two batches in the CLICIT and CLOCIT facilities at the Oregon State University TRIGA reactor (Table 1). Argon was released from sample aliquots of 0.5–4 mg by step-wise heating using the defocused beam of a CO_2 laser. To reach most homogeneous heating of the grains possible with this technique, we ensured that grains were not stacked. The analyses were carried out using two MAP-215 mass spectrometers, each equipped with one analog electron multiplier at Berkeley Geochronology Center (Table 1). Several samples were analyzed in duplicate to optimize the heating schedule for better separation of isotopic reservoirs. We scanned for double-charged ^{82}Kr on m/z 41 to monitor possible interference from double-charged ^{80}Kr on m/z 40, produced from Br during irradiation (Rutte et al., 2017); no significant contents were measured. Correction factors for collateral Ar isotope production and $^{37}Ar_{Ca}/^{39}Ar_K$ production ratio for CLICIT irradiation are taken from Renne et al. (2015); correction factors for CLOCIT are from Rutte et al. (2018), and we determined and used a $^{37}Ar_{Ca}/^{39}Ar_K$ production ratio of 1.99 ± 0.08 for CLOCIT using Hb3Gr in irradiation 476.

We define plateau dates by at least three contiguous steps that overlap within 2σ uncertainty, yield >50% of the released $^{39}Ar_K$, and have homogeneous Ca/K ratios. Plateau dates are calculated as inverse variance weighted means.

3.3. $^{40}Ar/^{39}Ar$ Age Interpretations

As in our results, previous $^{40}Ar/^{39}Ar$ studies employing stepwise-degassing analysis of Franciscan phengite and amphibole found partially disturbed age spectra; disturbances mostly stem from excess ^{40}Ar (radiogenic ^{40}Ar, separated from its parent ^{40}K) and the difficulty of preparing pure mineral separates from fine grained and sometimes intergrown phengite and amphiboles (Ross & Sharp, 1988; Wakabayashi & Dumitru, 2007). In most cases, reliable plateau or isochron ages can be calculated based on a subset of steps, but these deviate from the spectrum-integrated (also referred to as total fusion) ages. Early K/Ar and $^{40}Ar/^{39}Ar$ total fusion data from low-grade metasedimentary units of the Franciscan were comprehensively appraised by Dumitru et al. (2010). However, for lack of internal verifiability and testability of excess ^{40}Ar, we exclude all previous total fusion data from our discussion of the metamorphic blocks.

3.4. Laser-Ablation Split Stream (LASS) Zircon U-Pb Geochronology and Trace-Element Geochemistry

Samples were crushed, sieved, and washed with deionized water. Zircons were concentrated from about 2 kg of <150 μm sieve fraction using magnetic separation and heavy liquids. Though we attempted to isolate zircon from several more samples with ≤15 μm sized zircon visible in thin section, we were only able to retrieve zircons large enough for laser ablation from TIBB and BH-32. Zircon grains were handpicked in ethanol and mounted in epoxy, then polished to central sections and imaged using cathodoluminescence (CL) and backscattered electrons (BSE) detectors on an FEI Quanta 400f scanning electron microprobe at the University of California Santa Barbara (Figure S1).

Tectonics

10.1029/2020TC006305

Table 1
$^{40}Ar/^{39}Ar$ Data[a]

Sample	IGSN	MS	Lab-ID	Irradiation	Mineral	Grain size (μm)	IntA (Ma ± 2σ)	Plateau WMD (Ma ± 2σ)
BH-32	IEDRU0001	Nexus	18044-14	466_2	Hornblende	150–250	159.8 ± 2.0	**160.09 ± 0.92**
BH-32		Nexus	18056	466_3	White mica	250–355	146.0 ± 1.5	**146.26 ± 0.52**
BR-5	IEDRU0002	Nexus	18058-03	466_3	White mica	250–355	151.1 ± 1.5	150.8 ± 1.1
DRM-1	IEDRU0003	Nexus	18222-01	476PR_C	Hornblende	150–250	159.0 ± 3.9	**159.1 ± 1.4**
			18222-02				160.9 ± 3.5	**160.61 ± 0.94**
DRM-1		Nexus	18223	476PR_C	White mica	250–355	147.7 ± 1.9	147.5 ± 1.0
HR-2	IEDRU0004	Nexus	18057-01	466_3	White mica	250–355	140.9 ± 1.5	**140.53 ± 0.72**
			18057-02				141.9 ± 1.0	**141.94 ± 0.49**
HR-3	IEDRU0005	Nexus	18220-01	476PR_C	White mica	250–355	150.2 ± 1.0	148.9 ± 1.8
Je1r	IEDRU0006	Map 1	18071	466_4	Calcic amphibole	250–355	153.4 ± 1.3	**154.5 ± 2.3**
Je2	IEDRU0007	Map 1	18069	466_4	Hornblende	150–250	163.70 ± 0.74	159.85 ± 0.32
Je3d	IEDRU0008	Map 1	18070	466_4	Calcic amphibole	150–250	137 ± 44	**158 ± 14**
MH-3	IEDRU0009	Nexus	18216-01	476PR_C	Hornblende	190–300	144.5 ± 2.6	**153.1 ± 1.4**
			18216-02				142.4. ± 2.5	**154.0 ± 1.0**
MH-3		Nexus	18217	476PR_C	White mica	250–355	148.8 ± 1.8	**148.37 ± 0.67**
PG14	IEDRU000A	Map 1	18045-01	466_2	Hornblende	150–250	147.7 ± 3.1	**154.6 ± 1.4**
			18045-02				147.61 ± 0.59	NA
PG23	IEDRU000B	Nexus	18041-03	466_2	Hornblende	190–300	156.71 ± 0.55	**158.93 ± 0.91**
			18041-04				160.3 ± 2.6	**160.2 ± 1.8**
PG23		Map 1	18059	466_3	White mica	150–250	157.1 ± 1.6	156.80 ± 0.54
TIBBvein	IEDRU000C	Nexus	18230-03	476PR_C	White mica	212–350	156.8 ± 1.7	155.29 ± 0.63
RM-8	IEDRU000D	Map 1	18046-13	466_2	Hornblende	190–300	154.5 ± 1.6	**156.61 ± 0.86**
RM-8		Map 1	18054-01	466_3	White mica	150–250	155.1 ± 1.5	**155.35 ± 0.50**
YU4	IEDRU000E	Nexus	18219-01	476PR_C	White mica	100–200		

[a]MS, mass spectrometer; WMD, weighted mean date; IID, inverse isochron date; MSWD, mean square weighted deviation; WM, weighted mean. [b]EPMA data in Table S3. [c]Only steps with homogeneous Ca/K included

Tectonics

10.1029/2020TC006305

Table 1
Continued

Sample	Ca/K plateau steps	Ca/K EPMA[b]	IID (Ma ± 2σ)	Steps incl. in IIA (out of)	MSWD of IIA	$^{40}Ar/^{36}Ar$ (II) (2σ)	Age interpretation (Ma ± 2σ)
BH-32	18–20	15–24	160.3 ± 1.1	1–16 (16)	0.73	294 ± 12	**160.09 ± 0.92**; crystallization or cooling close to peak *T*
BH-32	0.00	NA	146.36 ± 1.96	1–15 (15)	0.25	291 ± 10	**146.26 ± 0.52**; blueschist-facies retrogression
BR-5	0.0	NA	**148.5 ± 1.4**	**3–15 (15)**	1.3	495 ± 88	**148.5 ± 1.4**; blueschist-facies retrogression
DRM-1	23–26	18–34	161.3 ± 2.8	1–16 (16)	1.7	283 ± 15	**160.14 ± 0.78**; WM of WMAs,
	23–26	18–34	158.9 ± 2.7	2–18 (18)	1.2	297 ± 16	Crystallization or cooling close to peak *T*
DRM-1	< 0.01	NA	**146.8 ± 2.3**	**3–13 (13)**	4.2	357 ± 74	**146.8 ± 2.3**; blueschist-facies retrogression
HR-2	< 0.1	NA	140.05 ± 0.84	1–15 (15)	1.7	302 ± 14	**141.23 ± 0.46;** WM of WMAs; vein crystallization
	< 0.1	NA	141.22 ± 0.65	1–15 (15)	2.4	294 ± 22	
HR-3	< 0.1	NA	**147.8 ± 3.0**	**4–13 (13)**	4.5	349 ± 57	**147.8 ± 3.0**; blueschist-facies retrogression
Je1r	63–82	25–40	155.1 ± 2.4	1–9 (9)	6.8	296.3 ± 3.9	**154.5 ± 2.3**; crystallization of rind
Je2	30–34	≥14	**158.1 ± 1.6**	**1–9 (9)**	15	313.8 ± 5	**158.1 ± 1.6**; crystallization or cooling close to peak *T*
Je3d	29–38	NA	167 ± 22	1–14 (14)	1.6	290.5 ± 8.9	**156 ± 17**; crystallization or cooling close to peak *T*
MH-3	10–13	NA	131 ± 14[c]	7–18 (18)	1.4	1,500 ± 1900	**153.70 ± 0.81**; disturbed spectrum,
	11–13	NA	154.1 ± 4.2[c]	7–18 (18)	1.5	280 ± 250	Minimum age of amphibole overprint
MH-3	< 0.01	NA	149.2 ± 2.7	4–13 (13)	6.1	290 ± 170	**148.37 ± 0.67;** blueschist-facies retrogression
PG14	19–23	18–45	145 ± 10	4–11 (11)	7	355 ± 89	**154.6 ± 1.4**; disturbed spectrum,
	21–23	NA	134 ± 21	4–16 (16)	200	480 ± 260	Minimum age of amphibole overprint
PG23	14–18	NA	159.26 ± 0.73	1–26 (26)	0.64	300 ± 23	**159.19 ± 0.81**; WM of WMAs,
	14–18	NA	159.8. ± 2.2	1–6 (6)	5.1	286.6 ± 6.6	Crystallization or cooling close to peak *T*
PG23	< 0.1	NA	**156.4 ± 1.1**	**1–15 (15)**	2.5	333 ± 24	**156.4 ± 1.1;** cooling age
TIBBvein	< 0.1	NA	**150.4 ± 2.9**	**4–17 (17)**	2.4	690 ± 180	**150.4 ± 2.9;** crystallization age of vein
RM-8	15–17	14–17	155.6 ± 2.4	3–15 (15)	7.5	240 ± 100	**156.61 ± 0.86**; crystallization or cooling close to peak T
RM-8	<0.02	NA	154.9 ± 1.1	3–16 (16)	0.27	319 ± 44	**155.35 ± 0.50**; blueschist-facies retrogression
YU4	<0.03	NA		NA	NA	NA	**>205**; blueschist-facies metamorphism

[a]MS, mass spectrometer; WMD, weighted mean date; IID, inverse isochron date; MSWD, mean square weighted deviation; WM, weighted mean. [b]EPMA data in Table S3. [c]Only steps with homogeneous Ca/K included

LASS analyses were performed at the University of California, Santa Barbara; U-Th-Pb isotopes and trace-element data were collected simultaneously on the same spot (Kylander-Clark et al., 2013). Samples were ablated using a Photon Machines 193 nm excimer laser with a HelEx ablation cell coupled to a Nu Instruments Plasma HR multicollector inductively coupled plasma mass spectrometer (MC-ICPMS) for U-Pb measurements, and an Agilent 7700X quadrupole ICPMS for trace-element analyses. ^{238}U and ^{232}Th were detected on Faraday cups whereas ^{204}Pb + Hg, ^{206}Pb, ^{207}Pb, and ^{208}Pb were collected on ion counters. All samples were run during the same analytical session. The laser was first fired with a 15–20 μm spot to remove surface contamination, and this material was allowed to wash out for 15 s. Material was then continuously ablated with a 15–20 μm spot for 75 shots at a 5 Hz repetition rate, yielding approximate pit depths of 4 μm. The laser fluence at the sample surface was identical for all experiments at ~0.8 J/cm^2. Analyses of unknowns were bracketed by analyses of matrix-matched zircon reference material (RM) 91500 (1062.4 ± 0.4 ID-TIMS ^{206}Pb/^{238}U date: Wiedenbeck et al., 1995), which was used as the primary RM for U-Pb isotopic analyses. Zircon RMs GJ-1 (601.7 ± 1.3 ID-TIMS ^{206}Pb/^{238}U date: Jackson et al., 2004; Kylander-Clark et al., 2013), Plešovice (337.13 ± 0.37 ID-TIMS ^{206}Pb/^{238}U date; Sláma et al., 2008), and Piexe (564 ± 4 Ma ID-TIMS ^{206}Pb/^{238}U date: Dickinson & Gehrels, 2003) were used as secondary standards, with GJ-1 further serving as the primary trace-element RM. Using the same parameters and methods applied to unknowns, we obtained ^{206}Pb/^{238}U concordia dates of 606.0 ± 3.8 Ma for GJ-1, 339.1 ± 3.5 Ma for Plešovice, and 571.7 ± 6.5 Ma for Piexe during the zircon analytical session, which are accurate to ~0.7%, ~1.4%, and ~0.6% of their reference values, respectively. For trace-element analyses, ^{90}Zr (assuming identical wt. % Zr in both sample and RM) was used as an internal standard, with measured peaks on the 7700X at ^{28}Si, ^{31}P, ^{49}Ti, ^{89}Y, ^{90}Zr, ^{140}Ce, ^{141}Pr, ^{146}Nd, ^{147}Sm, ^{153}Eu, ^{157}Gd, ^{159}Tb, ^{163}Dy, ^{165}Ho, ^{166}Er, ^{169}Tm, ^{172}Yb, ^{175}Lu, and ^{178}Hf, with Si, P, and Ti used as monitors for mineral inclusions within the zircons. Iolite plug-in version 2.21 (Paton et al., 2011) for the Wavemetrics Igor Pro software was used to correct measured isotopic ratios and elemental intensities for baselines, time-dependent laser-induced inter-element fractionation, plasma-induced fractionation, and instrumental drift. Downhole fractionation was modeled using an exponential best fit.

The uncertainty of single measurements is dominated by counting statistics and signal stability. Each ^{207}Pb/^{206}Pb and ^{206}Pb/^{238}U measurement requires an additional 2% error attributable to variation in ablation or transport characteristics, mass-balance instabilities, or plasma loading effects; this was added in quadrature. Long-term analysis shows that this equipment and method are capable of measuring the baseline- and fractionation-corrected ^{206}Pb/^{238}U and ^{207}Pb/^{206}Pb of a primary reference material (e.g., 91,500 zircon) with a long-term precision of ≤1.5% (Kylander-Clark et al., 2013). When combined with uncertainties in the isotopic ratios of the primary RM and U decay constants, the date of a homogeneous unknown has an external uncertainty of ~2%. All date uncertainties are reported at the 95% confidence interval, assuming a Gaussian distribution of measurement errors. Stated 2σ date uncertainties are internal; that is, they include propagated in-run and decay constant errors only. Low and imprecise Ti concentrations in zircon (coupled with uncertain silica activities) preclude robust temperature calculations for zircon (re)crystallization.

3.5. Comparability of Geochronologic Methods

We herein compare Lu-Hf, U-Pb, and ^{40}Ar/^{39}Ar data. The compiled Lu-Hf ages are calculated using a ^{176}Lu decay constant of 1.867 × 10^{-11}a^{-1} calibrated directly with the U-Pb system (Scherer, 2001; Söderlund et al., 2004). We therefore consider only the given Lu-Hf isochron uncertainties with the original data. The external uncertainty of the U-Pb method using our methods is ~2% (see above). New and compiled ^{40}Ar/^{39}Ar ages are calculated based on standard age and decay data intercalibrated with the U-Pb system using the optimization approach of Renne et al. (2010, 2011). Systematic uncertainties based on inconsistencies between the three decay systems fall below the time scales interpreted in this study.

4. Results: Block Descriptions and Analytical Data

In the following we describe data from individual blocks with respect to their locale, petrography, and results of previous studies on the same blocks. We then report our new geochronologic results and their context, followed by a brief interpretation of the data for the block. Comparisons among individual blocks, and overarching interpretations, follow in section 5. New ^{40}Ar/^{39}Ar and U-Pb results are displayed in Figures 3 and 4,

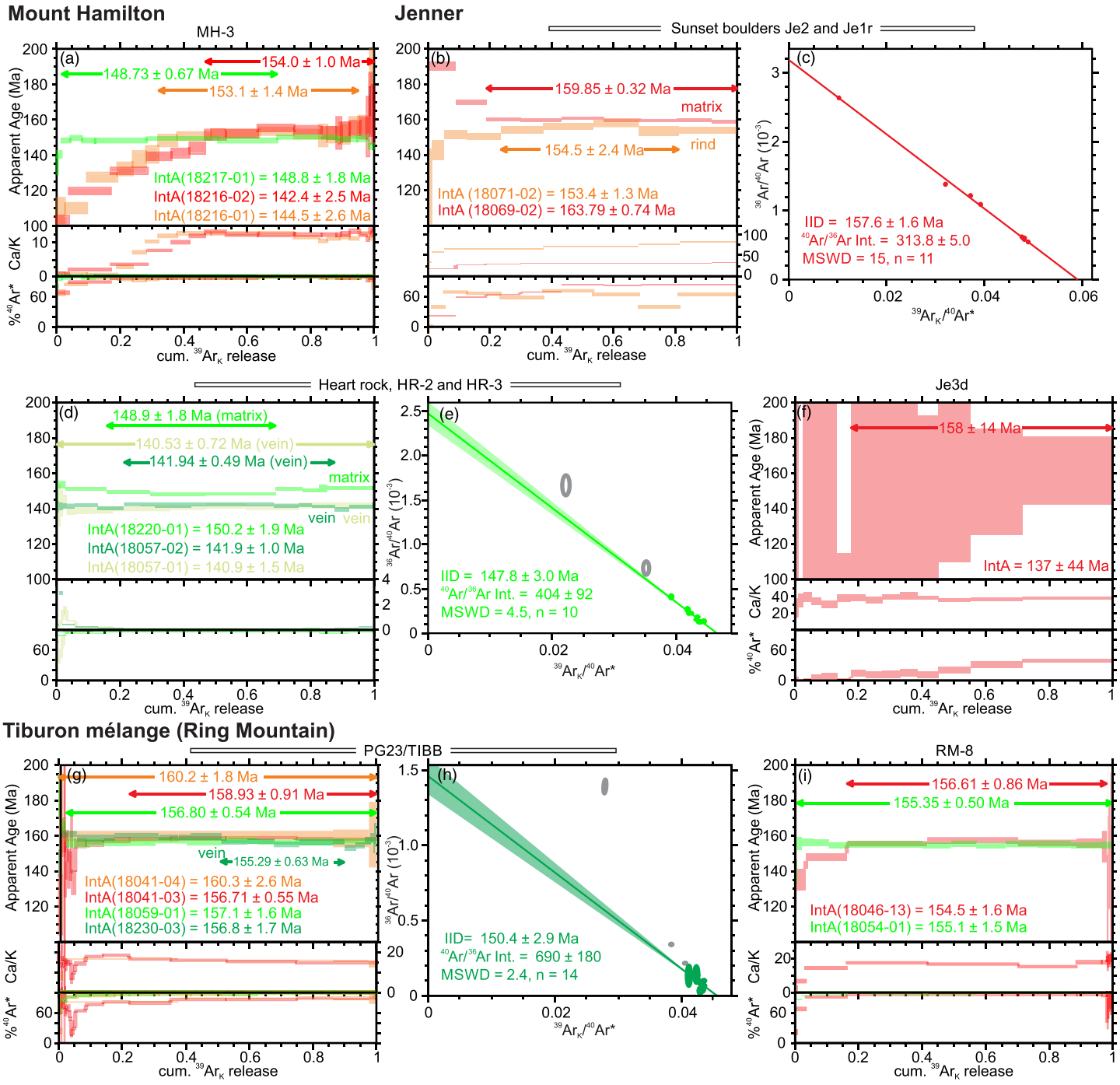

Figure 3a. $^{40}Ar/^{39}Ar$ geochronology results. Apparent age spectra with weighted mean ages and integrated gas ages (K-Ar equivalent) are reported for all samples and aided by inverse isochron plots for samples with complex $^{40}Ar/^{36}Ar$ compositions. Results from amphibole and phengite are in red and green tones, respectively. Uncertainties are plotted at the 1σ level, but calculated results are at the 2σ level for ease of comparability with other methods. Further analytical detail in Table 1 and supporting information. Abbreviations: IID, inverse isochron date; IntA, integrated age; Int., intercept; MSWD, mean square weighted deviation; cum., cumulative. Raw data used to construct these plots are in Table S1.

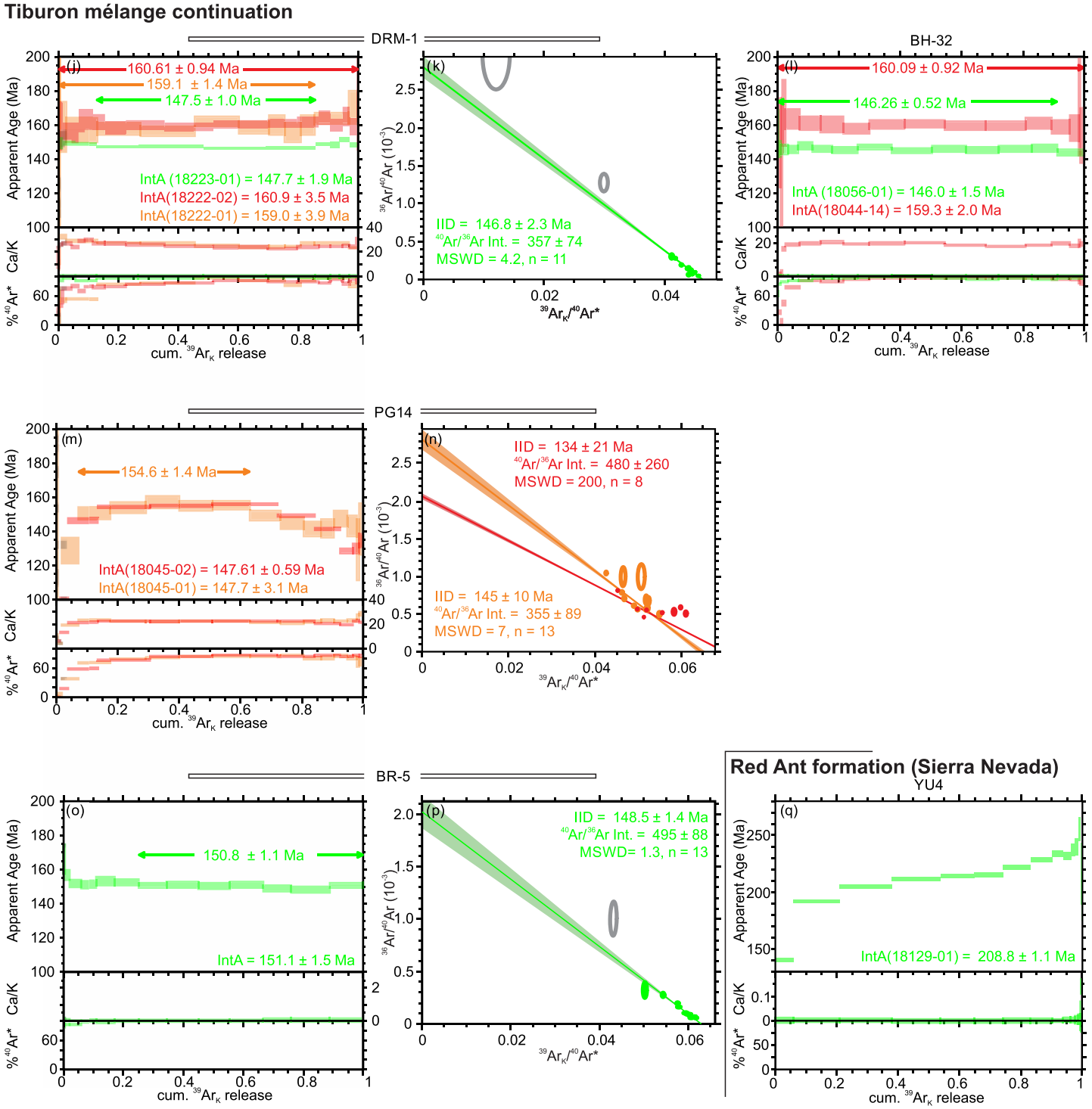

Figure 3b. (continued)

respectively. Figure S2 provides a photographic documentation of the samples and Table S1 electron probe microanalysis data of amphibole and phengite.

4.1. Mount Hamilton: MH-3

MH-3 was a block at the west slope of Mount Hamilton that was destroyed by a road crew in 1990. The block was composed of an eclogite core with lenses of garnet-amphibolite, wrapped by a retrograde metamorphic

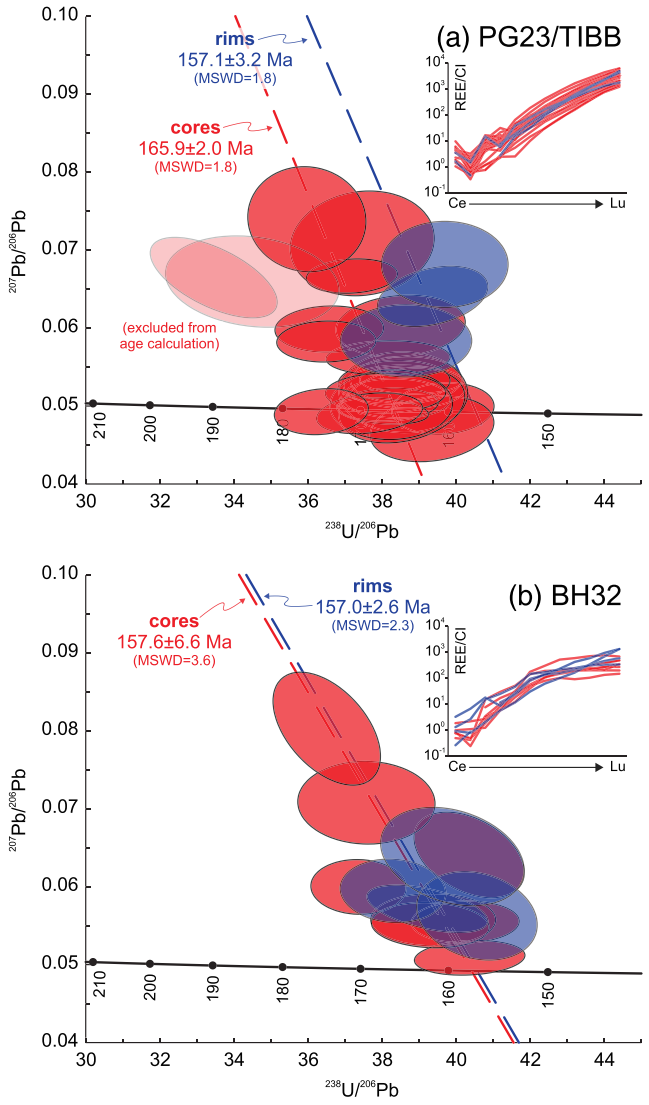

Figure 4. Summary of zircon results from samples BH-32 (a) and PG32/TIBB (b). Spot analyses, calculated isochrons, and chondrite-normalized rare-earth element (REE) plots are color-coded by texture (cores and rims). Two core spots from PG32/TIBB are clearly older and were excluded from the core isochron calculation in panel B. Chondrite values for REE normalization were sourced from McDonough and Sun (1995). Raw data used to construct these plots are in Table S2. Constructed using ISOPLOT (Ludwig, 2012).

rind. Catlos and Sorensen (2003) dated individual phengite crystals from the rind using laser ablation $^{40}Ar/^{39}Ar$ analysis with a weighted mean dates of 142.9 ± 3.7 Ma (their block MH-90). Two aliquots of hornblende from the garnet-amphibolite in MH-3 yielded similar rising apparent age spectra and Ca/K ratios in the beginning of the step-heating experiment (Figure 3a). The second half of released $^{39}Ar_K$ yielded plateau dates with a weighted mean date of 153.70 ± 0.81 Ma and stable Ca/K ratios of 10–13. Signals of ^{36}Ar are small, and the steps with homogeneous Ca/K have very little spread in inverse isochron space and thus define an imprecise date. The shape of age and Ca/K spectra and the comparably low Ca/K of the plateau date point to a successive homogenization of Ar from the hornblende and—likely—younger, low Ca/K phengite inclusions during the step-heating experiment, analogous to the observations of Ross and Sharp (1988). We thus interpret the weighted-mean date of 153.70 ± 0.81 Ma as a minimum age for crystallization or cooling of the hornblende. Phengite from the rind yielded a plateau date of 148.37 ± 0.67 Ma. The inverse isochron through the plateau steps yields a $^{40}Ar/^{36}Ar$ intercept of 290 ± 170 (i.e., atmospheric with no inherited Ar). We interpret the date as the age of crystallization or cooling of phengite.

4.2. Jenner: Sunset Boulders (Je1r and Je2)

Je1r and Je2 consist of multiple amphibolite fragments littered over a 100 × 60 m area. They were mapped atop the marine terrace south of the Russian River estuary by (Wakabayashi, 2015). Individual fragments are up to 15 × 10 × 10 m in size and are in some cases broken apart in place. Sample Je2 is an amphibolite sample from a central large fragment. It contains brown hornblende with a ferro-tschermakite to ferro-pargasite composition. Matrix hornblende (Je2) yields a plateau date of 159.85 ± 0.32 Ma with a Ca/K ratio of 30–34 (Figure 3b). An inverse isochron through all steps has a super-atmospheric $^{40}Ar/^{36}Ar$ intercept of 313.8 ± 5 and yields an inverse isochron date of 158.1 ± 1.6 Ma (Figure 3c). Because of the small component of excess Ar, we prefer the slightly younger inverse isochron date. Sample Je1r is a piece of chlorite-actinolite rind sampled from a fragment at the edge of the boulder field. Actinolitic amphibole from the rind yields a plateau date of 154.5 ± 2.3 with a Ca/K of 63–82 (Figure 2b). An inverse isochron through all steps has an atmospheric $^{40}Ar/^{36}Ar$ intercept. The dates are indistinguishable within uncertainty and permit three possible interpretations: (i) both dates are cooling ages, (ii) both dates are crystallization ages, or (iii) the matrix hornblendes date cooling during crystallization of the rind.

4.3. Jenner: Heart Rock (HR-2 and HR-3)

Heart Rock is a 3 × 5 × 4 m sized block of epidote + garnet-blueschist at Jenner Beach. Foliation parallel mineralogical layering is isoclinally folded and cut by veins of phengite and sodic amphibole. Remain of clinopyroxene were found in garnet, suggesting earlier eclogite-facies metamorphism (Carruthers & Rowe, 2017). Phengite from the matrix yields 3.4 Si pfu. It yields a subtly saddle shaped $^{40}Ar/^{39}Ar$ age spectrum with a plateau date of 148.9 ± 1.8 Ma (Figure 3d). An inverse isochron through steps 4–13 yields a $^{40}Ar/^{36}Ar$ intercept of 349 ± 57 (atmospheric within uncertainty) and an inverse isochron date of 147.8 ± 3.0 Ma (Figure 3e). Steps 1–3, however, bend toward a nonatmospheric $^{40}Ar/^{36}Ar$ value. Because of this hint to excess ^{40}Ar, we prefer the inverse isochron date over the weighted-mean age and interpret it to be the age of crystallization or cooling through phengite closure to Ar diffusion. Microprobe analysis of phengite from a crosscutting vein yields an indistinguishable composition from the host rock; two

aliquots yielded plateau dates with atmospheric intercept of 283 ± 15 and 297 ± 16 and a resulting inverse variance weighted mean date of 141.49 ± 0.43 Ma, straightforwardly interpreted as the age of formation of the vein (Figure 3d). Together, the phengite host-rock and vein dates indicate a residence time of ≥6 Ma in the blueschist facies.

4.4. Jenner: Je3d

Je3d is from a 35 × 30 × 20 m sized block of garnet blueschist atop the marine terrace south of the Russian River estuary. The sample consists of—in thin section—mostly blue to purple amphibole with complex optical zonation patterns and few greenish amphibole grains, possibly indicating an earlier amphibole-eclogite facies metamorphism (Figure S2). We were able to separate only few dark greenish (in separate) amphibole grains with low K-content and thus obtained comparably imprecise data. The sample yields a $^{40}Ar/^{39}Ar$ plateau date of 158 ± 14 Ma (Figure 3f). An inverse isochron through all steps yields an atmospheric $^{40}Ar/^{36}Ar$ intercept of 290.5 ± 8.9.

4.5. Tiburon Mélange: PG23/TIBB/TIBBvein

PG23 is a 3 × 3× > 2 m large garnet- and phengite-bearing amphibolite block from Ring Mountain that was first described by Wakabayashi, 1990; his sample TIBB). Phengite and hornblende define the main penetrative foliation and stretching lineation. Rare fold hinges preserve an older isoclinally folded foliation with the axial planes parallel to the main foliation. Omphacite-rich eclogite occurs in bands and patches throughout the block. Wakabayashi (1990) described eclogite "veins" crosscutting the foliation defined by the hornblende and concluded that the higher-pressure eclogite assemblage overprints the older hornblende paragenesis. A reevaluation of the data led Tsujimori et al. (2006; their sample A) to peak *P-T* conditions of the eclogite assemblage (Grt-Cpx-Phe) of 550–620°C at 1.9–2.5 GPa and interpretation of a hairpin *P-T* path in which retrograde and prograde metamorphism followed a similar trajectory. Cooper et al. (2011) calculated peak *T* of 510–560°C for the amphibolite paragenesis (Grt-Hbl). Varying modes of chlorite and glaucophane indicate variable retrograde overprint of both amphibolite and eclogite assemblages. During sampling we discovered a previously undescribed vein of coarse phengite (>10 mm) and bladed gray-blue amphibole aggregates (>20 mm long) cross cutting the foliation (sample TIBBvein; Figure S2). Saha et al. (2005) analyzed the bulk rock chemistry of PG23 (their sample TIBB), found little indication of trace-element mobility since crystallization, and interpreted the sample protolith as a nascent arc basalt. Anczkiewicz et al. (2004) determined a Lu-Hf garnet-WR date of 153.4 ± 0.8 Ma from a two-point isochron (their sample PG23).

Zircons from a garnet-amphibolite layer are up to 150 μm in length, but mostly <100 μm long and have a compact habit with aspect ratios around 1:2. Cathodoluminescence reveals patchy zoning, with bright rims overgrowing darker and partially metamict cores along lobate boundaries (Figure S1). However, zircon cores and rims share a similar mineral chemistry; core and rim Th/U ratios range from 0.2–0.8 and 0.4–0.5, respectively, and cores and rims have similar REE abundances without a statistically significant Eu anomaly (Figure 4a, inset; Table S2). Core analyses range from concordant to a few percent discordant, and an isochron regression through 22 spot analyses yields a lower-intercept $^{206}Pb/^{238}U$ date of 165.9 ± 2.0 Ma (MSWD = 1.8; Figure 4a; cf. Wendt & Carl, 1991). Two core spots yielded much older dates of ~180–185 Ma, albeit with significant uncertainties (±10 Ma) and with trace-element compositions indistinguishable from other core analyses. Only three inclusion-free rim spots were obtained; using the same upper intercept defined by the core isochron ($^{207}Pb/^{206}Pb \approx 0.5$), we obtain a lower-intercept $^{206}Pb/^{238}U$ rim date of 157.1 ± 3.2 Ma (MSWD = 1.8; Figure 4a). A rim isochron calculated using the Stacey and Kramers (1975) $^{207}Pb/^{206}Pb$ for the calculated date (~0.85) yields the same date within uncertainty. We also attempted titanite and rutile U-Pb dating from this sample, but uranium concentrations for both minerals were below the LA-ICP-MS detection limit.

Two aliquots of matrix hornblende yield well defined $^{40}Ar/^{39}Ar$ plateau dates with a weighted mean date of 159.19 ± 0.81 Ma (Figure 3g). Inverse isochrons through all steps yield $^{40}Ar/^{36}Ar$ intercepts of 300 ± 23 and 286.6 ± 6.6. Phengite from the matrix yields a plateau date of 156.80 ± 0.54 Ma with a slightly supra-atmospheric $^{40}Ar/^{36}Ar$ intercept of 333 ± 24. We thus prefer the slightly younger inverse isochron date of 156.4 ± 1.1 Ma. Phengite from the coarse vein yields a similar apparent age spectrum but with a downward step in the middle. In inverse isochron space the first three steps describe a bend toward atmospheric

$^{40}Ar/^{36}Ar$, while the following 14 steps form an inverse isochron with a $^{40}Ar/^{36}Ar$ intercept of 690 ± 180 and a date of 150.4 ± 2.9 Ma (Figure 3h).

These dates and mineral chemistry data implicate metamorphic (re)crystallization of zircon cores without coexisting plagioclase from at least 166 Ma until 158 Ma; if the older zircon core dates (~180 Ma) are significant, they may record protolith basalt crystallization, or alternatively suggest a much earlier initiation of eclogite-facies conditions. Because the eclogite-facies assemblages define the main, penetrative foliation, the observed isoclinal folding must have occurred during this prograde metamorphic interval. With the calcic hornblende having grown along the prograde path (Wakabayashi, 1990), and a peak *T* of 550–620°C exceeding the hornblende Ar closure temperature (Tsujimori et al., 2006), the $^{40}Ar/^{39}Ar$ dates of hornblende dates are straightforwardly interpreted as cooling close to peak *T* conditions at ~159 Ma, synchronous with zircon resorption and rim growth. The $^{40}Ar/^{39}Ar$ plateau date of matrix phengite is the age of cooling below phengite Ar closure at ~157 Ma. The $^{40}Ar/^{39}Ar$ inverse isochron date of vein phengite is the age of vein crystallization at ~150 Ma from an aqueous fluid carrying inherited ^{40}Ar. Considering these constraints, the TIBB block spent at least ~7 Ma (and potentially up to ~20 Ma) under high-grade prograde conditions and remained at blueschist facies or higher conditions for another ~8 Ma in the subduction zone.

4.6. Tiburon Mélange: RM-8

RM-8 is a 5 × 12× > 2 m large epidote-garnet-amphibolite block on Ring mountain that was first detailed by Mulcahy et al. (2014). Phengite and hornblende define a strong foliation and stretching lineation. No variation in lithology or internal structure is visible given a comparably fresh and lichen free level of exposure. Late carbonate-filled fractures are oriented perpendicular to the long axis of the block. Mulcahy et al. (2014) determined a peak *T* of 636 ± 46°C by modeling Ca and Mg zonation in garnet and obtained a Lu-Hf garnet-WR date of 153.4 ± 0.8 Ma from a 6-point isochron.

Matrix hornblende is zoned with magnesio-hornblende, magnesio-taramite, barroisite, and actinolite compositions in grain cores, overgrown by ferroan glaucophane rims. Microprobe analysis yielded Ca/K ratios ranging 14 to 17 in hornblende and above 160 in sodic amphiboles. Matrix hornblende yielded a $^{40}Ar/^{39}Ar$ plateau date of 156.61 ± 0.86 Ma at a Ca/K of 15–17 (Figure 3i) with an atmospheric $^{40}Ar/^{36}Ar$ of 240 ± 100 of the inverse isochron. We interpret this to be the age of retrograde hornblende crystallization or cooling through Ar closure in hornblende. In either case the date is most likely close to determined peak *T* conditions. Phengite yielded 3.4 Si pfu and a $^{40}Ar/^{39}Ar$ plateau date of 155.35 ± 0.50 Ma. In inverse isochron space, steps 3–15 form an isochron with an atmospheric $^{40}Ar/^{36}Ar$ intercept of 319 ± 44. We interpret this date to be the age of cooling or crystallization of phengite with minor incorporation of excess ^{40}Ar in the blueschist facies. We attempted titanite and rutile U-Pb dating, but U concentrations were too low for LA-ICP-MS analysis.

4.7. Tiburon Mélange: DRM-1/EA

DRM-1 is a 20 × 25× > 6 m large block on Ring mountain that was first described by Mulcahy et al. (2018; their sample EA). Its dominant lithology is a phengite and garnet-bearing amphibolite, with a penetrative foliation and stretching lineation defined by hornblende and phengite. Up to 40 mm thick and 5 m long layers of garnetite are found subparallel to the foliation; Mulcahy et al. (2018) found a symmetric chemical zonation inside the garnetite layers and suggested syntaxial growth in a successively opening fracture.

Zircons included in garnet and from the matrix yielded lower intercept inverse concordia dates of 176.5 ± 3.8 Ma and 160.3 ± 3.2 Ma, respectively (Mulcahy et al., 2018). These were interpreted as ages of early prograde—probably eclogite-facies—metamorphism at ~176 Ma, followed by hornblende paragenesis overprinting at ~160 Ma. Mulcahy et al. (2018) further analyzed garnet compositions and found variable zoning patterns suggesting a complex growth and resorption history. Lu-Hf geochronology of multiple garnet aliquots reflects this observation by scattering in isochron space; isochrons enveloping all isotopic data were interpreted to date episodes of garnet growth from 166 ± 1 Ma to 155 ± 1 Ma (Mulcahy et al., 2018).

Two aliquots of matrix hornblende yielded plateau dates with a weighted mean of 160.14 ± 0.78 Ma (Figure 3j). Inverse isochrons yield atmospheric intercepts of 283 ± 15 and 297 ± 16. We interpret this to be the age of hornblende crystallization or cooling through Ar closure in hornblende. Phengite yields a

saddle shaped $^{40}Ar/^{39}Ar$ apparent age spectrum. In inverse isochron space, the first two steps bend toward an atmospheric $^{40}Ar/^{36}Ar$ intercept, while successive steps define an isochron with a date of 146.8 ± 2.3 Ma and a $^{40}Ar/^{36}Ar$ intercept of 357 ± 74 for steps 3–13 (Figure 3k). We interpret this date to be the age of cooling or crystallization of phengite under incorporation of minor amounts of excess ^{40}Ar.

4.8. Tiburon Mélange: BH-32

BH-32 is a 3 × 2 × 2 m sized block of garnet amphibolite in the Berkeley Hills. The block has weak foliation and stretching lineation and was described in detail by Mulcahy et al. (2018). It contains omphacite crystals included in garnet and as relicts within a matrix of sodic amphibole and hornblende. Garnets display complex zoning patterns indicating episodic growth and resorption. From these observations, Mulcahy et al. (2018) interpreted an initial eclogite-facies metamorphic event, followed by amphibolite paragenesis and blueschist-facies overprints. Lu-Hf isotopic compositions of multiple aliquots scatter in isochron space; Mulcahy et al. (2018) calculated enveloping isochrons and interpreted them to date episodic garnet growth between 172 ± 1 Ma and 156 ± 1 Ma.

Ten zircons from BH-32 have long axes of up to 120 μm with an elongated habit (aspect ratios ~1:3). Cathodoluminescence reveals up to 15 μm wide rims overgrowing cores along rounded boundaries in three grains (Figure S1); one core is metamict. The cores and rims have similar CL textures and have generally similar compositions with respect to Th/U, REE, and Eu/Eu*. However, the rim analyses typically have steeper HREE slopes than the core spots, which typically exhibit flat chondrite-normalized HREE patterns (Figure 4b, inset). Eight core analyses yield an imprecise unconstrained isochron (lower intercept $^{206}Pb/^{238}U$ date = 157.6 ± 6.6 Ma) that does not form a single population (MSWD = 3.6), with an upper intercept ($^{207}Pb/^{206}Pb \approx 0.38$) that deviates significantly from the Stacey and Kramers (1975) value for the same date ($^{207}Pb/^{206}Pb = 0.85$). Using the same upper intercept as determined by the core isochron regression, four rim analyses yield a statistically significant isochron date of 157.0 ± 2.6 Ma (MSWD = 2.3) (Figure 4b). The synchronicity between core and rim zircon dates, coupled with changes in REE slope—and their similarity to the youngest garnet Lu-Hf dates from the same sample (Mulcahy et al., 2018)—suggests that the zircon growth and recrystallization textures relate to the cessation of garnet growth and the initiation of garnet breakdown by ~157 Ma.

In thin section, hornblende tends to have darker cores and lighter rims or patchy zoning and overgrowth of sodic amphibole. EPMA-determined amphibole compositions include barroisite, edenite, magnesio-hornblende, and magnesio-katophorite with Ca/K ratios ranging 15–24. Our hornblende separate yields a $^{40}Ar/^{39}Ar$ plateau date of 160.09 ± 0.92 Ma at a relatively constant Ca/K of 18–20 (Figure 3l). An inverse isochron through all steps yields an atmospheric intercept. Phengite yields 3.4 Si pfu and a $^{40}Ar/^{39}Ar$ plateau date of 146.26 ± 0.52 Ma. An inverse isochron through all steps yields an atmospheric $^{40}Ar/^{36}Ar$ intercept.

The garnet and zircon data suggest that high-grade metamorphism started prior to ~170 Ma with episodes of garnet and zircon (re)crystallization until ~157 Ma. The hornblende date at ~159 Ma could be interpreted as a cooling age or crystallization age, in either case during retrogression, but close to peak *T*. The phengite Ar/Ar date can be either interpreted as a cooling age or crystallization age during blueschist-facies retrogression. Prograde metamorphism thus lasted >11 Ma and later blueschist facies metamorphism continued for >15 Ma.

4.9. Tiburon Mélange: PG14

PG14 is a 40 × 40 × 30 cm sized block of garnet amphibolite in the Berkeley Hills. It is foliated and has a stretching lineation defined by hornblende; ≤1 mm wide calcite veins cut the block. Anczkiewicz et al. (2004) determined metamorphic peak-T of 580–610°C from garnet-hornblende thermometry, and a garnet crystallization age of 162.5 ± 0.5 Ma from a 4-point garnet-WR Lu-Hf isochron.

Amphiboles have a patchy zoning with magnesio-hornblende and barroisite compositions and overgrowths of actinolite. Microprobe analyses yield Ca/K ratios ranging 18–45. Two aliquots yielded similar but complex $^{40}Ar/^{39}Ar$ apparent age spectra with an initial rise from ~45 Ma to ~154 Ma, decreasing again to ~130 Ma (Figure 3m). The Ca/K ratios determined from $^{37}Ar_{Ca}/^{39}Ar_K$ rise in parallel to the rising apparent ages to ~22, form a plateau and only the last steps show another increase. In inverse isochron space, individual steps exhibit excess scatter suggesting mixture of one nonradiogenic and two radiogenic sources (Figure 3n). The

complex apparent age and Ca/K spectra likely relate to differential degassing and phase changes of the magnesio-hornblende and barroisite during the step-heating experiment (cf. Wartho et al., 1991). We consider the plateau date of aliquot 1 at 154.6 ± 1.4 Ma to be a minimum age for the cooling of hornblende through Ar-closure.

4.10. Tiburon Mélange: BR-5 (Big Rock)

Big Rock is a 10 × 12 × 12 m sized garnet-epidote blueschist block near Nicasio, CA. It is probably part of the Tiburon mélange. Mulcahy et al. (2014) determined peak *T* conditions of 542 ± 41°C from garnet cation diffusion zonation assuming a pressure of 10 kbar and further determined a 4-point Lu-Hf garnet-WR isochron date of 156.2 ± 1.0 Ma. Sample BR-5 contains remnants of hornblende in the matrix (Mulcahy et al., 2014), but we found these grains to be inseparable from phengite and did not attempt to date them. We found sodic amphibole, but no hornblende inclusions in garnet.

Phengite from BR-5 contains 3.4 Si pfu. It yields a subtly saddle shaped apparent age spectrum with a plateau date of 150.8 ± 1.1 Ma (Figure 3o). An inverse isochron through steps 3–15 yields a super-atmospheric $^{40}Ar/^{36}Ar$ intercept of 495 ± 88, indicating the presence of excess Ar, and a date of 148.5 ± 1.4 Ma (Figure 3p). Steps 1 and 2 bent toward an atmospheric intercept, likely related to adhered atmospheric Ar. We prefer the inverse isochron date over the plateau date and interpret it as the age of crystallization or cooling during retrograde blueschist facies metamorphism. The presence of sodic amphibole and the lack of hornblende inclusions in the previously dated garnet suggests that amphibolite-facies metamorphism occurred prior to ~156 Ma (Figure S2).

4.11. Red Ant Schist: YU4

To explore the significance of earlier K/Ar dates—which suggested a temporal correlation between early Franciscan subduction and suturing in the Sierra foothills—we performed $^{40}Ar/^{39}Ar$ analysis of phengite from one of the outcrops investigated by Schweickert et al. (1980) at the Yuba River near Downieville, outside our main study area. Phengite from sample YU4 yielded a complex apparent age spectrum rising from 140 Ma to mostly 205–220 Ma with Ca/K _x0003C; 0.007 (Figure 3q). The last steps yield apparent ages rising up to 256 Ma with a Ca/K rising to 0.03. The integrated age, approximately equivalent to a conventional K/Ar date for our sample, is 208.1 ± 1.1 Ma. Our new $^{40}Ar/^{39}Ar$ data highlight the difficulty of interpreting legacy K/Ar dates; it shows that phengite in the Red Ant schist records a complex thermal history and suggests that blueschist-facies metamorphism in the western Sierra foothils is older than ~205 Ma and thus unrelated to early Franciscan subduction.

5. Discussion

5.1. Timescales of Metamorphism of High-Grade Blocks

The application of multiple geo- and thermochronometers to individual blocks allows us to discriminate the duration of metamorphism that each block experienced, from (i) prograde-to-peak crystallization of garnet and zircon, to (ii) retrograde hornblende crystallization or cooling, to (iii) retrograde blueschist-facies phengite crystallization or cooling. These data allow comparison among blocks from different parts of the Franciscan Complex, including an understanding of whether the blocks were subducted and exhumed as part of a coherent package, and how the duration and absolute timing of retrograde metamorphism varied locally and regionally. As a first observation, red and blue boxes in Figure 2b highlight the absence of coeval prograde (grt and zircon dates) and retrograde (mostly hornblende and phengite dates) eclogite facies metamorphism along regions of the Franciscan subduction zone; this discrimination is broadly synchronous along the entire orogen. In the following we discuss the overall interpretation of the $^{40}Ar/^{39}Ar$ dates of hornblende and phengite, their regional variability, and then compare the results of multiple methods applied to individual blocks.

While phase relations strongly suggest that the PG23 $^{40}Ar/^{39}Ar$ hornblende date is a cooling age, in all other samples the hornblende date may be the age of cooling or crystallization; nonetheless, a succinct interpretation is possible. Calculated peak *T* conditions of the amphibolites are in the range of 500–600°C. Growth of hornblende *sensu lato* in metabasite during subduction metamorphism requires temperatures above ~470°C (Ernst, 1979; Hernández-Uribe & Palin, 2019). For retrograde hornblende growth, kinetics likely limit (re) crystallization to even higher *T*. A simple diffusion model of hornblende for representative width of 200–

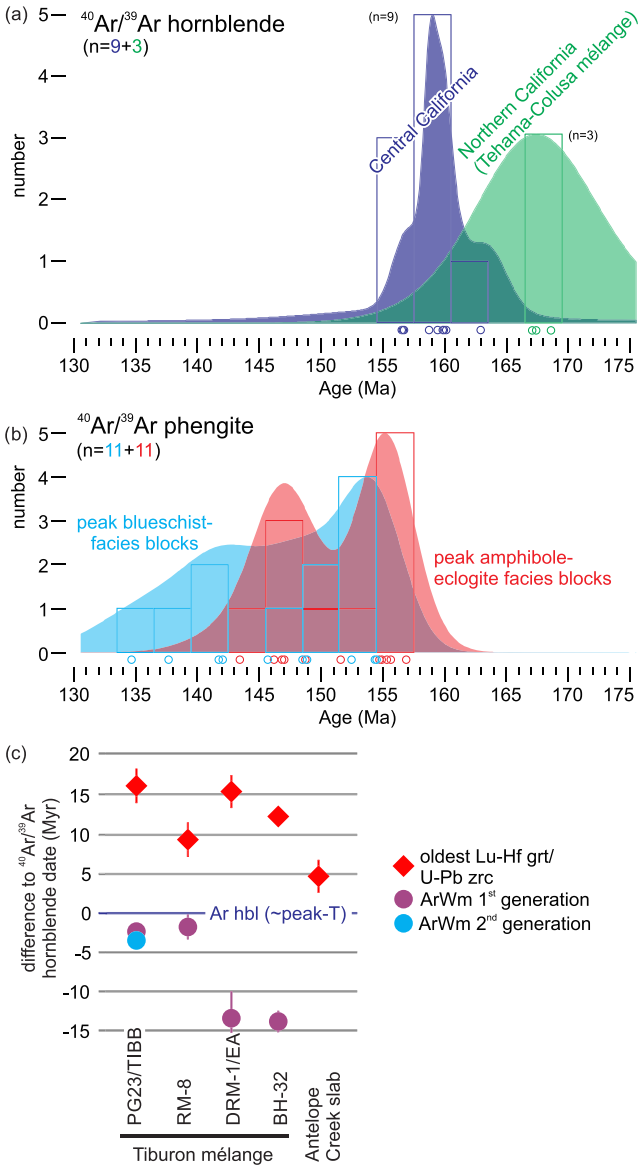

Figure 5. Distribution of geochronometric data. (a) and (b) Published and new ^{40}Ar/^{39}Ar amphibole and phengite ages from high-grade blocks and amphibole-eclogite facies coherent units displayed in histograms and kernel-density estimate curves (cf. Vermeesch, 2012). A narrow range of high-confidence ^{40}Ar/^{39}Ar amphibole dates suggests a punctuated phase of cooling in the amphibolite facies with a younging trend from northern to central California. In contrast, wide range of ^{40}Ar/^{39}Ar phengite dates suggests prolonged cooling and recrystallization in the blueschist facies. (c) Timescales of metamorphism relative to ^{40}Ar/^{39}Ar hornblende dates which approximate the age of peak *T* metamorphism.

500 μm (infinite cylinder) and cooling rates of 10–100°C/Ma suggests closure temperature of Ar in hornblende of 507–589°C (Brandon et al., 1998; Harrison, 1981). With peak *T*, minimum (re)crystallization temperature and closure temperature converging at 500–600°C, we propose that—be they cooling or crystallization ages—the ^{40}Ar/^{39}Ar hornblende dates are a minimum—but close—estimate of the age of peak *T* metamorphism.

The durations between ^{40}Ar/^{39}Ar hornblende and matrix phengite dates range 1.2–14 Ma. The shortest difference in RM-8 with 1.2 ± 1.0 is difficult to interpret because both dates may date cooling or crystallization. In contrast, the hornblende and matrix phengite dates of sample PG23 are straightforwardly interpreted as cooling ages (see above). Matrix phengite is 2.8 ± 1.4 Ma younger than the ^{40}Ar/^{39}Ar hornblende date. Assuming closure temperatures of ~550°C for hornblende at fast cooling rates and ~360°C for phengite (Wijbrans et al., 1993; Wijbrans & McDougall, 1986) points to cooling rates of 45–136°C/Ma for a few Ma time interval. In the other samples, phengite dates may be the age of crystallization, in which case the dates can be linked to temperatures ≤360°C (less than the closure temperature of Ar in phengite). Durations of 13.3 ± 2.4 and 13.8 ± 1.1 Ma between ^{40}Ar/^{39}Ar hornblende and ^{40}Ar/^{39}Ar matrix phengite of DRM-1 and BH-32 indicate slower average cooling rates of ~15°C/Ma. Crystallization of a second generation of phengite in veins and rinds in PG23, MH-3, and HR2&3 indicates that blueschist-facies metamorphism lasted at least another 6.0 ± 1.1, 5.3 ± 4.1, and 6.6 ± 3.0 Ma, respectively. In general, the scatter of ^{40}Ar/^{39}Ar phengite dates is larger than that of ^{40}Ar/^{39}Ar hornblende dates (Figures 2b and 5a).

Our new and compiled ^{40}Ar/^{39}Ar hornblende dates point to a distinct phase of block cooling from 168 to 157 Ma (n = 12; Figures 2b, 5a, and 5b, two disturbed dates excluded). When considering the dates in respect to their paleolatitudinal position a north-to-south younging trend is apparent. The oldest 168–166 Ma (n = 3) dates stem from the Tehama-Colusa mélange in northern California. The Antelope Creek slab from central California east of the San Andreas fault system—with an intermediate geographic position prior to Cenozoic strike-slip motion (reconstruction based on Wakabayashi, 1999)—has a date of 163.3 ± 2.1 Ma (Ross & Sharp, 1988). The samples from Ward Creek and Jenner were at a similar latitude, whereas those from Ring Mountain and the Berkeley Hills were further south during Franciscan subduction, and range from 160.14 ± 0.78–156.61 ± 0.86 Ma (n = 8; Figure 5). This trend may be tested in the future by geochronologic analysis of high-grade blocks from the Sixes River mélange in Oregon that likely represents the northward continuation of the mélanges studied in California (Coleman & Lanphere, 1971) and would extend the study area by 350 km (Figure 1). In contrast to the tight clustering of the ^{40}Ar/^{39}Ar hornblende dates, ^{40}Ar/^{39}Ar phengite dates are more variable, ranging between 156.4 ± 1.1 and 134.6 ± 0.4 (n = 24; Figure 5) with most samples at 155–140 Ma. Considering only the blocks and coherent units that experienced amphibole-eclogite facies metamorphism (i.e., excluding those samples with peak *P-T* conditions in the blueschist facies), the range remains at 156.4 ± 1.1–143.4 ± 3.7 Ma (n = 12). All phengite data stem from Central California and do not allow comparison with the N-S trend observed in the hornblende data. The varying range of ^{40}Ar/^{39}Ar hornblende and phengite dates indicate relatively uniform initial exhumation of the high-grade

blocks and coherent units from the amphibole-eclogite facies during a 5–10 Ma interval. In contrast, retrograde blueschist-facies metamorphism was prolonged and varied over >15 Ma (Figures 2b, 5a, and 5b).

To further compare durations of metamorphism based on multiple geochronometer we use the $^{40}Ar/^{39}Ar$ matrix hornblende dates to approximate the age of peak *T* conditions. Figure 5c shows the difference between the matrix hornblende $^{40}Ar/^{39}Ar$ date with the oldest available prograde metamorphic age (Lu-Hf garnet or U-Pb zircon), matrix phengite $^{40}Ar/^{39}Ar$ date and (if present) any second phengite generation in a vein or rind. This estimate returns durations of prograde metamorphism of 5–18 Ma. However, only a rough estimate of the metamorphic conditions dated by the garnet and zircon is possible. While two ~180 Ma zircon dates in samples PG23 (Figure 4a) may reflect protolith (igneous) processes, most of the zircon U-Pb dates in this study overlap with Lu-Hf or Ar/Ar dates from the same samples (Figure 2), suggesting that zircon ages are intimately related to metamorphic (re)crystallization. There is no evidence that these zircons grew from in situ melts, or that these blocks ever experienced suprasolidus conditions. Our interpretation is supported by trace-element data tied to each U-Pb age. For example, the absence of a negative europium anomaly ($Eu/Eu^* < 1$) in zircons is commonly interpreted to indicate the crystallization in a plagioclase-free, eclogitic assemblage (e.g., Rubatto & Hermann, 2003). However, it should be noted that plagioclase often is only an accessory phase in the investigated blocks and in Franciscan amphibolites in general (e.g., Wakabayashi, 1990). The positively sloping chondrite-normalized HREE patterns for all investigated zircons (Figure 4) suggest that zircon crystallized prior to garnet crystallization or after garnet breakdown, that the amount of garnet in equilibrium with zircon was insufficient to deplete the bulk rock in HREE, or that zircon REE uptake was governed by local rather than bulk-rock factors.

Garnet occurs in a range of Franciscan blueschists with peak-*T* conditions as low as 400°C, such that Lu-Hf dates may record a range of prograde-to-peak metamorphic conditions. Additionally, available Lu-Hf garnet dates have been accompanied by a characterization of major-element zonation of the garnets (Anczkiewicz et al., 2004; Cooper et al., 2011; Mulcahy et al., 2014, 2018) but did not include documentation of Lu distribution within the garnets. Further, Moore et al. (2013) showed that REE distributions in undated Franciscan garnets are exceedingly complex, far more so than represented by the major element data. Therefore, the limited information prevents robustly determining if the Lu-Hf dates represent mostly early, late, or mixed growth intervals. Though most Franciscan Lu-Hf data define single isochrons, the isotopic data of samples BH-32 and DRM-1 span an age range and their complex elemental zoning point to a complex growth and resorption history (Mulcahy et al., 2018).

All of the above-discussed complexities discourage a detailed direct comparison of the apparently variable duration of prograde metamorphism between blocks. However, the apparent long prograde-to-peak metamorphic durations of >15 Ma for blocks that reached ~600°C (PG23, DRM-1), that is, ~15 Ma for ~300°C of heating at 20°C/Ma, point to a relatively slow sinking rate of ~18 km/Ma, assuming an intermediate geothermal gradient of 11°C/km (discussed below in more detail). Even considering that $^{40}Ar/^{39}Ar$ hornblende ages may partially postdate peak-metamorphism by few Ma, or considering that zircon and garnet growth may have started at lower *T*—that is, both resulting in slight underestimation of the actual rate—it is at the lower limit of known sinking rates of 12–100 km/Ma in established modern subduction zones (England et al., 2004; Jarrard, 1986). Either the subduction rate was slow, or the sampled rocks were decoupled during prograde slab sinking and dragged down at a lower rate than the remainder of the slab. Further, detailed quantitative petrologic investigation is required to reveal the *P-T* conditions dated by the Lu-Hf method and to test whether the blocks share a similar subduction rate.

In summary, our findings point to a lengthy progression of these blocks at high *P* and *T*, followed by relatively uniform cooling at ≤136°C/Ma at amphibole-eclogite facies conditions. Blueschist facies lower-*T* cooling became nonuniform and slowed to ~15°C/Ma with a potential residence time.

5.2. Deformation and Rind Formation

Early isoclinal folding and late fracturing has been observed in multiple Franciscan high-grade blocks including the herein studied PG23 (eclogite/amphibolite; Tsujimori et al., 2006) and Heart Rock (epidote-blueschist; Carruthers & Rowe, 2017). The isoclinal folding of PG23 occurred under prograde amphibole-eclogite facies conditions (Tsujimori et al., 2006; this study). Ages of phengite bearing crosscutting veins in Heart Rock and TIBB indicate blueschist facies fracturing of the blocks during exhumation

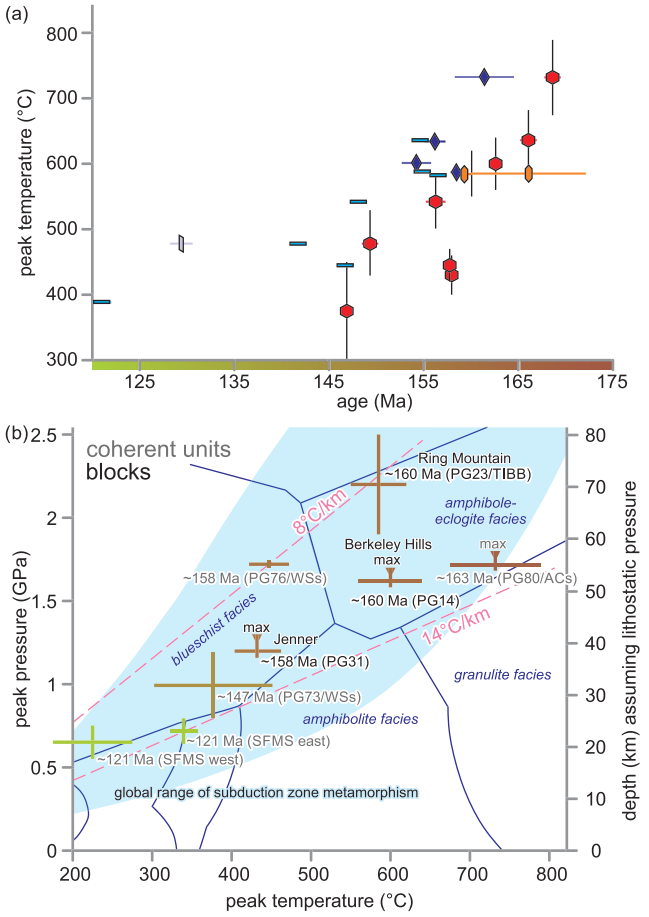

Figure 6. Pressure-Temperature-Time evolution of high-grade units. (a) *t-T* diagram showing dates of geochronometers of individual blocks as a function of the peak-*T* determined for the block. Symbology adapted from Figure 2. A correlation of older ages with peak-T reached by the blocks was previously interpreted to indicate cooling of the subduction zone assuming similar exhumation depth (Cooper et al., 2011). (b) *P-T* diagram showing peak *P-T* data of blocks and coherent units along with the approximate age of peak metamorphism, estimated between prograde Lu-Hf garnet or U-Pb zircon and retrograde $^{40}Ar/^{39}Ar$ hornblende or phengite dates. The arrows indicate maximum pressure estimates. Blocks and coherent units metamorphosed between 121 and 170 Ma, span the entire range of geothermal gradients, and do not support the cooling subduction zone model of Cooper et al. (2011). To the contrary, younger metamorphism after ~157 Ma exhibited higher average geothermal gradients. Range of known *P-T* conditions in subduction zones is from Penniston-Dorland et al. (2015). WSs, Willow Spring slab; ACs, Alder Creek Slab; SFMS, South Fork Mountain schist.

and lack of significant ductile deformation after ~141 and ~150 Ma, respectively. For the Sunset boulders block, our data indicate that the actinolite-chlorite rind formed approximately at the time of retrograde hornblende paragenesis overprinting, prior to 154.5 ± 2.3 Ma. This is in line with the results of Catlos and Sorensen (2003). Depending on the interpretation of the rind as having formed at the block periphery or as internal selvage (section 2.2), it indicates encasement in a serpentinite matrix or imbrication with serpentinite during retrogression. Current understanding of the rheology of metabasites and serpentinites does not allow for isoclinal folding of the former in a matrix of the latter, because metabasites are significantly stronger than serpentinized peridotite (Okazaki & Hirth, 2020; Proctor & Hirth, 2016). The chronology of deformation and rind formation thus indicates that PG23 and (possibly all blocks) were part of larger coherent units at the time of prograde metamorphism, underwent plastic deformation to varying degrees, and were encased in or intercalated with serpentinite only during exhumation and retrogression.

5.3. Do the Blocks and Coherent Slabs Record Cooling of the Subduction Zone?

Anczkiewicz et al. (2004), Cooper et al. (2011), and Mulcahy et al. (2014) compared peak temperatures and metamorphic ages of blocks and coherent terranes. They found that the oldest blocks (dated by Lu-Hf garnet) preserved the highest temperatures and interpreted this trend to result from a slowly subducting and slowly cooling subduction zone (Figure 6a). Numerical models of an initiating subduction zone best fit the trend for a slow subduction rate of ~10 km/Ma (Cooper et al., 2011). Evaluating the expanded *P-T-t* dataset sheds a different light: In *P-T* space (Figure 6b), the blocks and coherent slabs with quantitative *P* and *T* estimates span a field with average geothermal gradients ranging 8–14°C/km, covering most of the observed global range of subduction zone metamorphism (Figure 6b; cf. Penniston-Dorland et al., 2015). Both coherent slabs and blocks span the full range of average geothermal gradients. The ages of prograde to peak metamorphism determined here and elsewhere do not support an overall cooling geothermal gradient in the subduction zone from 170–120 Ma. On the contrary, the units metamorphosed after ~158 Ma (blueschist portion of Willow Spring slab and South Fork Mountain schist) preserve average geothermal gradients in the *hotter* portion of the observed range. We recognize that quantitative pressure constraints for these metabasites are limited and often rely on quite general constraints and that the instantaneous Franciscan geotherm represents a balance between the thermal state of the incoming and overlying plates (e.g., Wakabayashi, 2015). However, given the available data, our collated observations support a scenario in which the average geothermal gradient of the Franciscan subduction zone did not significantly change, or even subtly increased, after ~158 Ma.

5.4. Tectonic Implications

The slow and potentially variable tempo of prograde metamorphism of the high-grade blocks and coherent units with sinking rates ≤18 km/Ma can be explained by either subduction rates at the slow end of modern subduction zones or early decoupling of the units from the downgoing plate as proposed by the circular block-in-mélange flow model after Gerya et al. (2002). However, additional observations leave the hypothesis of metabasite block subduction to eclogite facies conditions and exhumation from there inside a circular flow

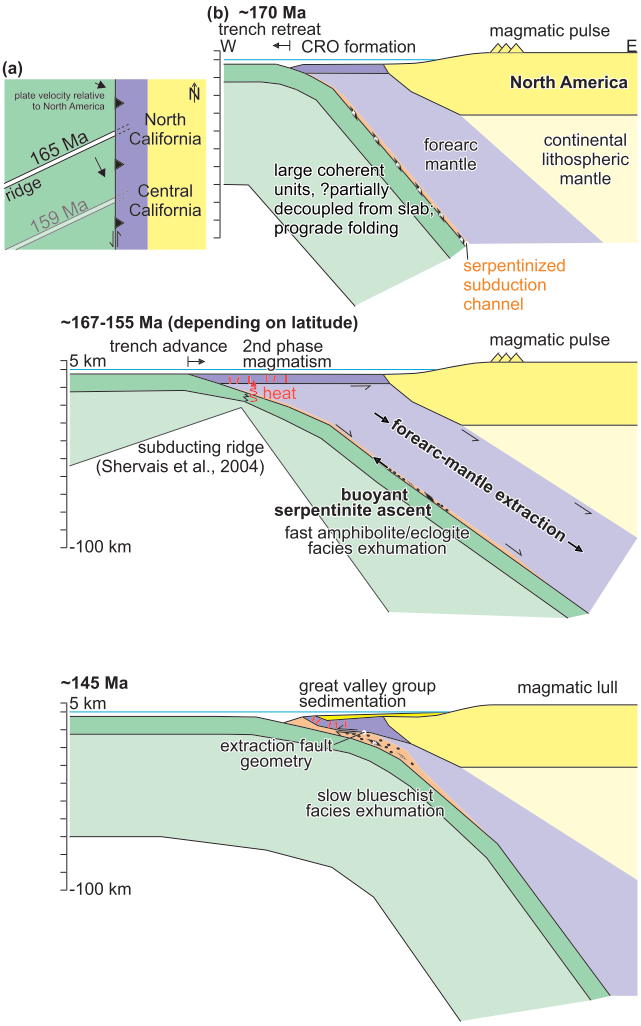

Figure 7. Proposed tectonic evolution of the early Franciscan subduction zone system. (a) The map shows a plate configuration in which a spreading ridge subducts beyond the Franciscan trench. The ridge-trench-trench triple junction moves south over time. (b) After initiation at ~170 Ma the subduction zone rolled back and the CRO formed along the retreating trench. Coherent units of metabasites subducted at a slow rate and were partly isoclinally folded. At ~160 Ma ridge subduction (Shervais et al., 2004) or near-trench approach of a ridge (Wakabayashi, 2017b) with young buoyant crust forced trench advance and sheared the CRO crust of its forearc mantle. The forearc mantle—assumed to have a high density—then sank at a higher rate compared to the subducting slab resulting in forearc mantle extraction and exhumation of the slab. Fragmentation of coherent units began forming the high-grade blocks. Buoyant serpentine ascent likely aided exhumation. Forearc mantle extraction allows exhumation of the blocks without them passing through the thermal anomaly above the subducting ridge. By 150 Ma the blocks were exhumed into the blueschist facies and welded beneath the CRO crust along an extraction fault. Following exhumation was slower and may have occurred along discrete faults. CRO, Coast Range ophiolite.

mélange unsubstantiated: (1) The prograde isoclinal folding observed in some blocks later encased in a weaker serpentinite matrix indicates that they were still parts of larger (coherent) units during subduction, which is further supported by (2) the lack of documented prograde metamorphic rind formation. This may still be consistent with a version of the model in which plucking of metabasite from the slab occurs only at peak conditions. However, prediction of a "chaotic" timing of progression and retrogression (predicted by circular mélange flow models) is not substantiated, as (3) there is little evidence for prolonged, coeval prograde and retrograde amphibole-eclogite-facies metamorphism among different blocks and (4) punctuated, event-like, high-grade exhumation contradicts the predicted "chaotic" timing of progression and retrogression (Figure 2b). Instead, we suggest that the eclogite/amphibolite blocks were subducted at very slow rates and as coherent units—maybe part of the downgoing slab—that experienced significant differential stresses and deformation during the initial ~15 Ma of the Franciscan subduction zone.

The regionally uniform cooling of blocks and coherent sheets from peak-temperatures to <500°C has an event-like character (Figure 2b). This high-grade part of the retrogression varies along strike from ~165 Ma in northern California to 160–157 Ma in central California. Our data suggest forcing of the onset of exhumation by a feature in the subducting plate that asynchronously entered the subduction zone. Besides the above discussed exhumation of blocks-in-mélange relative to the boundaries of the mélange, four exhumation mechanisms have been previously proposed for exhumation of the Franciscan Complex: (1) extrusion of material driven by relatively low-density serpentinite from beneath the forearc mantle (Ernst, 1970; Wakabayashi, 2017a), which can be similar to (2) extrusion of a wedge bounded by a thrust below and a normal fault above (Maruyama et al., 1996), (3) normal faulting (Platt, 1986), and (4) erosion and thrust faulting (Ring & Brandon, 1994; see also Wakabayashi, 1999, for critique).

Mechanisms 3 and 4 explain exhumation within an accretionary wedge, i.e., in the blueschist facies. They cannot explain the initial exhumation from depths up to 80 km, particularly under the absence of a significantly large accretionary wedge at the time. Assuming buoyant ascent or extrusion (mechanisms 1 and 2) of serpentinite is responsible for exhuming eclogite-facies units, what may have caused this process to have occurred for only a brief phase at ~160 Ma, but not before or after? A prominent change in the subduction zone proposed for this time is the subduction of a ridge interpreted to explain near-trench, late-stage magmatism observed in the CRO that occurred at 157–150 Ma (Hopson et al., 2008; Shervais et al., 2004; Figure 7). Subduction of the successively younger crust toward an active ridge would change the dip and bending radius of the subduction zone and thus of the buoyancy of weak material in the subduction channel (Mancktelow, 1995). The absence of a thermal overprint of the blocks suggests that they did not pass through the thermal anomaly created by the subducting ridge near the trench, that is, they did not exhume to near surface conditions in one step. Instead they were only exhumed to an intermediate depth as long as the thermal anomaly persisted (Figure 7). This agrees with our observation of a decreasing cooling rate in the blueschist facies.

Today the CRO overlies the Franciscan Complex along a >60 km (perpendicular to strike) long contact without intermittent forearc (CRO) mantle (Constenius et al., 2000). To explain the petrologic and

geochronologic data and modern crustal structure we propose forearc-mantle extraction as an additional (or alternative) exhumation mechanism to buoyant ascent, for the initial high-grade exhumation of eclogite/amphibolite units into the blueschist facies. In this context, the forearc-mantle wedge beneath the CRO and above the subducting Franciscan slab detached off the CRO crust when a relatively buoyant subducting ridge entered the subduction zone. The forearc mantle then sank, due to its relatively higher density (Figure 7). We define forearc mantle extraction as the forearc mantle being removed at a higher motion rate compared to the subducting slab resulting in differential exhumation of the slab. In this respect it differs from forearc mantle erosion where the subducting slab has a higher relative downward velocity.

The apparent increase of the average geothermal gradient documented in blueschist-facies units exhumed after ~157 Ma (Figure 7) and the initially low sinking rate are also plausible with a subducted ridge, particularly due to younging of the subducting oceanic crust. The Franciscan Complex at ~160 Ma may thus be analogous to the proposed extraction of the forearc mantle between the Yuli Belt and the Coastal Range of Taiwan after its detachment from the Philipine sea plate (Sandmann et al., 2015; Shyu et al., 2011). There, the anticipated trigger for the detachment and extraction was the buoyant Chinese continental margin entering the subduction zone.

After exhumation into the blueschist facies and welding to the base of the CRO crust, cooling/exhumation rates decreased and became more variable because discrete faults or shallowly operating subduction channel return flow became responsible for further exhumation (Platt, 1986; Ring & Brandon, 1994; Ukar & Cloos, 2019). Formation of the present-day outcropping mélanges involved further tectonic and sedimentary mixing after exhumation from the amphibole-eclogite facies into the blueschist facies by ~150 Ma (Wakabayashi, 2011, 2012, 2015). The lack of exhumation of any rocks higher-grade than blueschist facies metamorphosed after ~157 Ma supports our interpretation that the exhumation of amphibole-eclogite facies units was a punctuated effect related to a geodynamic anomaly, and not a steady-state process in the nascent Franciscan subduction zone. Similar interpretations have been drawn in other subduction zones, for example, in the Zagros in Iran (Agard et al., 2006)—suggesting that exhumed subduction-zone rocks may provide unrepresentative snapshots of the thermal and geodynamic structure compared to modern subduction zones.

Our expansion of the chronologic understanding of Franciscan subduction initiation and timing of high-grade exhumation correlates with other significant tectonic events within the Cordilleran chain. Initiation of Franciscan subduction prior 175 Ma correlates with accretion of the Quesnellia island arc in the Canadian cordillera and initiation of magmatism in the Talkeetna arc in southern Alaska. High-grade exhumation in the Franciscan subduction zone at ~160 Ma follows shortening and ophiolite obduction in the north Alaskan Brooks range and was followed by overthrusting of the Josephine ophiolite in the Klamath Mountains. Though these connections are preliminary, further high-precision geochronologic work on the precise timing of processes in circum-Pacific regions—along with geodynamic modeling—may allow genetic linkages between these apparently correlated geodynamic changes.

6. Conclusion

We can draw the following conclusions regarding the *P-T-t* history of individual blocks and coherent units:

1. Units subducted into the amphibole-eclogite facies were only exhumed during the first ~20 Ma (180–160 Ma) after Franciscan subduction initiation.
2. Prograde metamorphism of some units lasted ≥15 Ma suggesting slow sinking rates ≤18 km/Ma.
3. Chlorite-actinolite rinds formed in the amphibole-eclogite facies by ≥155 Ma, indicating high-grade exhumation of the blocks occurred in contact with serpentinite.
4. Exhumation of metabasites from the amphibole-eclogite facies was fast and occurred in a narrow time window at 168–157 Ma with a southward younging trend. It was a punctuated process that coincided with tectonomagmatic discontinuities in the Franciscan subduction system and the circum-Pacific subduction systems.
5. Exhumation of high-grade units slowed in the blueschist facies and became more variable (comparing different units) with the duration between $^{40}Ar/^{39}Ar$ hornblende and phengite dates ranging 1.2–14 Ma.
6. The herein expanded *P-T-t* data set for Franciscan high-grade units does not support a previously interpreted cooling of the subduction zone. To the contrary, units exhumed after ~157 Ma yield subtly higher average geothermal gradients.

Contrary to previous speculations, metamorphism in the Sierra foothills Red Ant schist along the Melones shear zone is significantly older and temporally unrelated to Franciscan subduction initiation. Our findings indicate that the exhumation of eclogites and amphibolites in the Franciscan Complex was triggered by a geodynamic one-time event rather than a continuous steady-state process. We propose that forearc-mantle extraction may best explain the available observations made in the Franciscan subduction system at ~160 Ma.

Data Availability Statement

All analytical data are accessible via OSF.IO/Q3GJN.

Acknowledgments

D. R. thanks John Wakabayashi for introduction to Franciscan geology during the 2016 Structural Geology and Tectonics Forum, Sarah Roeske for joint microprobe analysis, Samantha Carruthers and Christie Rowe for joint field work in Jenner, Nikolaus Froitzheim for instructive discussions, Sean Mulcahy for sharing sample BR-5, and John Platt for sharing thin sections. Microprobe data were evaluated using spread sheets online (www.gabbrosoft.org). General research support was provided by the Ann and Gordon Getty Foundation. We thank John Wakabayashi and Trevor Dumitru for thoughtful and detailed reviews that improved the clarity of the manuscript. D. R. was funded by the Deutsche Foschungsgemeinschaft (DFG, German Research Foundation)—287320649 and 421790087. J. M. G. acknowledges support from National Science Foundation Grant EAR-1219942 and from the University of California, Santa Barbara.

References

Agard, P., Monié, P., Gerber, W., Omrani, J., Molinaro, M., Meyer, B., et al. (2006). Transient, synobduction exhumation of Zagros blueschists inferred from P-T, deformation, time, and kinematic constraints: Implications for Neotethyan wedge dynamics. *Journal of Geophysical Research*, *111*, B11401. https://doi.org/10.1029/2005JB004103

Agard, P., Plunder, A., Angiboust, S., Bonnet, G., & Ruh, J. (2018). The subduction plate interface: Rock record and mechanical coupling (from long to short timescales). *Lithos*, *320-321*(November), 537–566. https://doi.org/10.1016/j.lithos.2018.09.029

Agard, P., Yamato, P., Jolivet, L., & Burov, E. (2009). Exhumation of oceanic blueschists and eclogites in subduction zones: Timing and mechanisms. *Earth-Science Reviews*, *92*(1–2), 53–79. https://doi.org/10.1016/j.earscirev.2008.11.002

Anczkiewicz, R., Platt, J. P., Thirlwall, M. F., & Wakabayashi, J. (2004). Franciscan subduction off to a slow start: Evidence from high-precision Lu-Hf garnet ages on high grade-blocks. *Earth and Planetary Science Letters*, *225*(1–2), 147–161. https://doi.org/10.1016/j.epsl.2004.06.003

Bailey, E. H., Blake, M. C. Jr, & Jones, D. L. (1970). *On-land Mesozoic oceanic crust in California Coast Ranges, U.S. Geological Survey Professional Paper* (Vol. *700*, pp. C70-C81). U.S. Geological Survey.

Bebout, G. E. (2007). Metamorphic chemical geodynamics of subduction zones. *Earth and Planetary Science Letters*, *260*(3–4), 373–393. https://doi.org/10.1016/j.epsl.2007.05.050

Blake, M. C., Engebretson, D. C., Jayko, A. S., & Jones, D. L. (1985). Tectonostratigraphic Terranes in Southwest Oregon. In *Tectonostratographic terranes of the Circum-Pacific Region* (pp. 147–157). CircumPacific Council Publications.

Brandon, M. T., Roden-Tice, M. K., & Garver, J. I. (1998). Late Cenozoic exhumation of the Cascadia accretionary wedge in the Olympic Mountains, northwest Washington State. *Geological Society of America Bulletin*, *110*(8), 985–1009. https://doi.org/10.1130/0016-7606(1998)110%3C0985:LCEOTC%3E2.3.CO;2

Carruthers, S., & Rowe, C. D. (2017). In C. D. Rowe (Ed.), *What can exhumed high grade blocks tell us about P-T and stress conditions along the subducting plate interface?* Paper presented at GAC/MAC Annual Meeting 2017.

Catlos, E. J., & Sorensen, S. S. (2003). Phengite-based chronology of K- and Ba-rich fluid flow in two paleosubduction zones. *Science (New York, N.Y.)*, *299*(January), 92–95. https://doi.org/10.1126/science.1076977

Cloos, M. (1982). Flow melanges: Numerical modeling and geologic constraints on their origin in the Franciscan subduction complex, California. *Geological Society of America Bulletin*, *93*(4), 330. https://doi.org/10.1130/0016-7606(1982)93<330:fmnmag>2.0.co;2

Cloos, M., & Shreve, R. L. (1988a). Subduction-channel model of prism accretion, melange formation, sediment subduction, and subduction erosion at convergent plate margins: 1. Background and description. *Pure and Applied Geophysics PAGEOPH*, *128*(3–4), 455–500. https://doi.org/10.1007/BF00874548

Cloos, M., & Shreve, R. L. (1988b). Subduction-channel model of prism accretion, melange formation, sediment subduction, and subduction erosion at convergent plate margins: 2. Implications and discussion. *Pure and Applied Geophysics PAGEOPH*, *128*(3–4), 501–545. https://doi.org/10.1007/BF00874549

Coleman, R. G., & Lanphere, M. A. (1971). Distribution and age of high-grade blueschists, associated eclogites, and amphibolites from Oregon and California. *Bulletin of the Geological Society of America*, *82*(9), 2397–2412. https://doi.org/10.1130/0016-7606(1971)82[2397:DAAOHB]2.0.CO;2

Constenius, K. N., Johnson, R. A., Dickinson, W. R., & Williams, T. A. (2000). Tectonic evolution of the Jurassic–Cretaceous Great Valley forearc, California: Implications for the Franciscan thrust-wedge hypothesis. *Geological Society of America Bulletin*, *112*(11), 1703–1723. https://doi.org/10.1130/0016-7606(2000)112%3C1703:TEOTJC%3E2.0.CO;2

Cooper, F. J., Platt, J. P., & Anczkiewicz, R. (2011). Constraints on early Franciscan subduction rates from 2-D thermal modeling. *Earth and Planetary Science Letters*, *312*(1–2), 69–79. https://doi.org/10.1016/j.epsl.2011.09.051

Cordova, J. L., Mulcahy, S. R., Schermer, E. R., & Webb, L. E. (2019). Subduction initiation and early evolution of the Easton metamorphic suite, northwest Cascades, Washington. *Lithosphere*, *11*(1), 44–58. https://doi.org/10.1130/L1009.1

Dickinson, W. R., & Gehrels, G. E. (2003). U–Pb ages of detrital zircons from Permian and Jurassic eolian sandstones of the Colorado Plateau, USA: Paleogeographic implications. *Sedimentary Geology*, *163*(1–2), 29–66. https://doi.org/10.1016/S0037-0738(03)00158-1

Dumitru, T. A., Wakabayashi, J., Wright, J. E., & Wooden, J. L. (2010). Early Cretaceous transition from nonaccretionary behavior to strongly accretionary behavior within the Franciscan subduction complex. *Tectonics*, *29*, TC5001. https://doi.org/10.1029/2009TC002542

England, P., Engdahl, R., & Thatcher, W. (2004). Systematic variation in the depths of slabs beneath arc volcanoes. *Geophysical Journal International*, *156*(2), 377–408. https://doi.org/10.1111/j.1365-246X.2003.02132.x

Ernst, W. G. (1970). Tectonic contact between the Franciscan Mélange and the Great Valley Sequence-Crustal expression of a Late Mesozoic Benioff Zone. *Journal of Geophysical Research*, *75*(5), 886–901. https://doi.org/10.1029/JB075i005p00886

Ernst, W. G. (1973). Blueschist metamorphism and P-T regimes in active subduction zones. *Tectonophysics*, *17*(3), 255–272. https://doi.org/10.1016/0040-1951(73)90006-1

Ernst, W. G. (1979). Coexisting sodic and calcic amphiboles from high-pressure metamorphic belts and the stability of barroisitic amphibole. *Mineralogical Magazine*, *43*(326), 269–278. https://doi.org/10.1180/minmag.1979.043.326.09

Ernst, W. G. (2011). Accretion of the Franciscan Complex attending Jurassic-Cretaceous geotectonic development of northern and central California. *Bulletin of the Geological Society of America*, *123*(9–10), 1667–1678. https://doi.org/10.1130/B30398.1

Evarts, R. C., Sharp, W. D., & Phelps, D. W. (1992). The Del Puerto Canyon remnant of the Great Valley ophiolite: Geochemical and age constraints on its formation and evolution. *Bulletin of the American Association of Petroleum Geologists*, *76*, 418.

Gerya, T. V., Stöckhert, B., & Perchuk, A. L. (2002). Exhumation of high-pressure metamorphic rocks in a subduction channel: A numerical simulation. *Tectonics*, *21*(6), 1056. https://doi.org/10.1029/2002TC001406

Ghatak, A., Basu, A. R., & Wakabayashi, J. (2012). Elemental mobility in subduction metamorphism: Insight from metamorphic rocks of the Franciscan Complex and the Feather River ultramafic belt, California. *International Geology Review*, *54*(6), 654–685. https://doi.org/10.1080/00206814.2011.567087

Hacker, B. R. (1993). Evolution of the northern Sierra Nevada metamorphic belt: Petrological, structural, and Ar/Ar constraints. *Geological Society of America Bulletin*, *105*(5), 637–656. https://doi.org/10.1130/0016-7606(1993)105%3C0637:EOTNSN%3E2.3.CO;2

Hacker, B. R. (2008). H 2 O subduction beyond arcs. *Geochemistry, Geophysics, Geosystems*, *9*, Q03001. https://doi.org/10.1029/2007GC001707

Hacker, B. R., & Goodge, J. W. (1990). Comparison of early Mesozoic high-pressure rocks in the Klamath Mountains and Sierra Nevada. In D. S. Harwood, & M. M. Miller (Eds.), *Paleozoic and Early Mesozoic paleogeographic relations: Sierra Nevada, Klamath Mountains, and related terranes* (Vol. 255, pp. 277–296). America: Geological Society of America. https://doi.org/10.1130/SPE255-p277

Hacker, B. R., Peacock, S. M., Abers, G. A., & Holloway, S. D. (2003). Subduction factory 2. Are intermediate-depth earthquakes in subducting slabs linked to metamorphic dehydration reactions? *Journal of Geophysical Research*, *108*(B1), 2030. https://doi.org/10.1029/2001JB001129

Hamilton, W. (1969). WARREN HAMILTON U.S. Geological Survey, Denver, Colorado 80225 Mesozoic California and the Underflow of Pacific Mantle. *GSA Bulletin*, *80*(December), 2409–2430. https://doi.org/10.1130/0016-7606

Harrison, M. T. (1981). Diffusion of ^{40}Ar in hornblende. *Contributions to Mineralogy and Petrology*, *78*(3), 324–331. https://doi.org/10.1007/BF00398927

Hermes, O. D. (1973). Paragenetic relationships in an amphibolitic tectonic block in the franciscan terrain, panoche pass, California. *Journal of Petrology*, *14*(1), 1–32. https://doi.org/10.1093/petrology/14.1.1

Hernández-Uribe, D., & Palin, R. M. (2019). A revised petrological model for subducted oceanic crust: Insights from phase equilibrium modelling. *Journal of Metamorphic Geology*, *37*(6), 745–768. https://doi.org/10.1111/jmg.12483

Hopson, C. A., Mattinson, J. M., Pessagno, E. A., & Luyendyk, B. P. (2008). California Coast Range ophiolite: Composite Middle and Late Jurassic oceanic lithosphere. *Special Paper 438: Ophiolites, Arcs, and Batholiths: A Tribute to Cliff Hopson*, *2438*(01), 1–101. https://doi.org/10.1130/2008.2438(01)

Hotz, P. E., Lanphere, M. A., & Swanson, D. A. (1977). Triassic blueschist from northern California and north-central Oregon. *Geology*, *5*(11), 659–663. https://doi.org/10.1130/0091-7613(1977)5%3C659:TBFNCA%3E2.0.CO;2

Ingersoll, R. V. (1978). Submarine fan facies of the Upper Cretaceous Great Valley sequence, northern and central California. *Sedimentary Geology*, *21*(3), 205–230. https://doi.org/10.1016/0037-0738(78)90009-x

Jackson, S. E., Pearson, N. J., Griffin, W. L., & Belousova, E. A. (2004). The application of laser ablation-inductively coupled plasma-mass spectrometry to in situ U-Pb zircon geochronology. *Chemical Geology*, *211*(1–2), 47–69. https://doi.org/10.1016/j.chemgeo.2004.06.017

Jarrard, R. D. (1986). Relations among subduction parameters. *Reviews of Geophysics*, *24*(2), 217. https://doi.org/10.1029/RG024i002p00217

Kohn, M. J., Castro, A. E., Kerswell, B. C., Ranero, C. R., & Spear, F. S. (2018). Shear heating reconciles thermal models with the metamorphic rock record of subduction. *Proceedings of the National Academy of Sciences*, *115*(46), 11,706–11,711. https://doi.org/10.1073/pnas.1809962115

Krogh, E. J., Oh, C. W., & Liou, J. C. (1994). Polyphase and anticlockwise P-T evolution for Franciscan eclogites and blueschists from Jenner, California, USA. *Journal of Metamorphic Geology*, *12*(2), 121–134. https://doi.org/10.1111/j.1525-1314.1994.tb00008.x

Kylander-Clark, A. R. C., Hacker, B. R., & Cottle, J. M. (2013). Laser-ablation split-stream ICP petrochronology. *Chemical Geology*, *345*, 99–112. https://doi.org/10.1016/j.chemgeo.2013.02.019

Ludwig, K. R. (2012). *User's manual for Isoplot 3.75, Berkeley Geochronology Center Special Publication* (Vol. *5*). Berkeley Geochronology Center.

MacPherson, G. J., Giaramita, M. J., & Phipps, S. P. (2006). Tectonic implications of diverse igneous blocks in Franciscan melange, Northern California and southwestern Oregon. *American Mineralogist*, *91*(10), 1509–1520. https://doi.org/10.2138/am.2006.2177

Mancktelow, N. S. (1995). Nonlithostatic pressure during sediment subduction and the development and exhumation of high pressure metamorphic rocks. *Journal of Geophysical Research*, *100*(B1), 571–583. https://doi.org/10.1029/94JB02158

Maruyama, S., Liou, J. G., & Terabayashi, M. (1996). Blueschists and Eclogites of the World and Their Exhumation. *International Geology Review*, *38*(6), 485–594. https://doi.org/10.1080/00206819709465347

McDonough, W. F., & Sun, S. S. (1995). The composition of the Earth. *Chemical Geology*, *120*(3–4), 223–253. https://doi.org/10.1016/0009-2541(94)00140-4

Metcalf, R. V., & Shervais, J. W. (2008). Suprasubduction-zone ophiolites: Is there really an ophiolite conundrum? *Special Paper 438: Ophiolites, Arcs, and Batholiths: A Tribute to Cliff Hopson*, *2438*(07), 191–222. https://doi.org/10.1130/2008.2438(07)

Moore, S. J., Carlson, W. D., & Hesse, M. A. (2013). Origins of yttrium and rare earth element distributions in metamorphic garnet. *Journal of Metamorphic Geology*, *31*(6), 663–689. https://doi.org/10.1111/jmg.12039

Mulcahy, S. R., King, R. L., & Vervoort, J. D. (2009). Lawsonite Lu-Hf geochronology: A new geochronometer for subduction zone processes. *Geology*, *37*(11), 987–990. https://doi.org/10.1130/G30292A.1

Mulcahy, S. R., Starnes, J. K., Day, H. W., Coble, M. A., & Vervoort, J. D. (2018). Early onset of Franciscan Subduction. *Tectonics*, *37*, 1194–1209. https://doi.org/10.1029/2017TC004753

Mulcahy, S. R., Vervoort, J. D., & Renne, P. R. (2014). Dating subduction-zone metamorphism with combined garnet and lawsonite Lu-Hf geochronology. *Journal of Metamorphic Geology*, *32*(5), 515–533. https://doi.org/10.1111/jmg.12092

Murphy, D. C., van der Heyden, P., Parrish, R. R., Klepacki, D. W., McMillan, W., Struik, L. C., & Gabites, J. (1995). *New geochronological constraints on Jurassic deformation of the western edge of North America, southeastern Canadian Cordillera* (pp. 159–172). https://doi.org/10.1130/SPE299-p159

Okazaki, K., & Hirth, G. (2020). Deformation of mafic schists from subducted oceanic crust at high pressure and temperature conditions. *Tectonophysics*, *774*(November 2019), 228217. https://doi.org/10.1016/j.tecto.2019.228217

Orme, D. A., & Surpless, K. D. (2019). The birth of a forearc: The basal Great Valley Group, California, USA. *Geology*, *47*(8), 757–761. https://doi.org/10.1130/G46283.1

Page, F. Z., Essene, E. J., Mukasa, S. B., & Valley, J. W. (2014). A garnet-zircon oxygen isotope record of subduction and exhumation fluids from the Franciscan Complex, California. *Journal of Petrology*, *55*(1), 103–131. https://doi.org/10.1093/petrology/egt062

Paterson, S. R., & Ducea, M. N. (2015). Arc magmatic tempos: Gathering the evidence. *Elements*, *11*(2), 91–98. https://doi.org/10.2113/gselements.11.2.91

Paton, C., Hellstrom, J., Paul, B., Woodhead, J., & Hergt, J. (2011). Iolite: Freeware for the visualisation and processing of mass spectrometric data. *Journal of Analytical Atomic Spectrometry*, *26*(12), 2508. https://doi.org/10.1039/c1ja10172b

Penniston-Dorland, S. C., Gorman, J. K., Bebout, G. E., Piccoli, P. M., & Walker, R. J. (2014). Reaction rind formation in the Catalina schist: Deciphering a history of mechanical mixing and metasomatic alteration. *Chemical Geology*, *384*, 47–61. https://doi.org/10.1016/j.chemgeo.2014.06.024

Penniston-Dorland, S. C., Kohn, M. J., & Manning, C. E. (2015). The global range of subduction zone thermal structures from exhumed blueschists and eclogites: Rocks are hotter than models. *Earth and Planetary Science Letters*, *428*, 243–254. https://doi.org/10.1016/j.epsl.2015.07.031

Platt, J. P. (1986). Dynamics of orogenic wedges and the uplift of high-pressure metamorphic rocks. *Geological Society of America Bulletin*, *97*(9), 1037–1053. https://doi.org/10.1130/0016-7606(1986)97%3C1037:DOOWAT%3E2.0.CO;2

Platt, J. P. (2015). Origin of Franciscan blueschist-bearing melange at San Simeon, central California coast. *International Geology Review*, *57*(5–8), 843–853. https://doi.org/10.1080/00206814.2014.902756

Proctor, B., & Hirth, G. (2016). "Ductile to brittle" transition in thermally stable antigorite gouge at mantle pressures. *Journal of Geophysical Research: Solid Earth*, *121*, 1652–1663. https://doi.org/10.1002/2015JB012710

Renne, P. R., Balco, G., Ludwig, K. R., Mundil, R., & Min, K. (2011). Response to the comment by W.H. Schwarz et al. on "Joint determination of 40K decay constants and $^{40}Ar^*/^{40}K$ for the Fish Canyon sanidine standard, and improved accuracy for $^{40}Ar/^{39}Ar$ geochronology" by P.R. Renne et al. (2010). *Geochimica et Cosmochimica Acta*, *75*(17), 5097–5100. https://doi.org/10.1016/j.gca.2011.06.021

Renne, P. R., Mundil, R., Balco, G., Min, K., & Ludwig, K. R. (2010). Joint determination of 40K decay constants and $^{40}Ar^*/^{40}K$ for the Fish Canyon sanidine standard, and improved accuracy for $^{40}Ar/^{39}Ar$ geochronology. *Geochimica et Cosmochimica Acta*, *74*(18), 5349–5367. https://doi.org/10.1016/j.gca.2010.06.017

Renne, P. R., Sprain, C. J., Richards, M. A., Self, S., Vanderkluysen, L., & Pande, K. (2015). State shift in Deccan volcanism at the Cretaceous-Paleogene boundary, possibly induced by impact. *Science*, *350*(6256), 76–78. https://doi.org/10.1126/science.aac7549

Ring, U., & Brandon, M. T. (1994). Kinematic data for the Coast Range fault and implications for exhumation of the Franciscan subduction complex. *Geology*, *22*(8), 735. https://doi.org/10.1130/0091-7613(1994)022%3C0735:KDFTCR%3E2.3.CO;2

Ross, J. A., & Sharp, W. D. (1988). The effects of sub-blocking temperature metamorphism on the K/Ar systematics of hornblendes: $^{40}Ar/^{39}Ar$ dating of polymetamorphic garnet amphibolite from the Franciscan Complex, California. *Contributions to Mineralogy and Petrology*, *100*(2), 213–221. https://doi.org/10.1007/BF00373587

Rubatto, D., & Hermann, J. (2003). Zircon formation during fluid circulation in eclogites (Monviso, Western Alps): Implications for Zr and Hf budget in subduction zones. *Geochimica et Cosmochimica Acta*, *67*(12), 2173–2187. https://doi.org/10.1016/S0016-7037(02)01321-2

Rutte, D., Becker, T. A., Deino, A. L., Reese, S. R., Renne, P. R., & Schickler, R. A. (2018). The new CLOCIT irradiation facility for $^{40}Ar/^{39}Ar$ geochronology: Characterisation, comparison with CLICIT and implications for high-precision geochronology. *Geostandards and Geoanalytical Research*, *42*(3), 301–307. https://doi.org/10.1111/ggr.12217

Rutte, D., Becker, T. A., & Renne, P. R. (2017). Quantifying interference of krypton produced from neutron irradiation of inclusion-hosted and lattice-coordinated bromine with $^{40}Ar/^{39}Ar$ geochronology. *Geochimica et Cosmochimica Acta*, *211*, 1–9. https://doi.org/10.1016/j.gca.2017.04.034

Saha, A., Basu, A. R., Wakabayashi, J., & Wortman, G. L. (2005). Geochemical evidence for a subducted infant arc in Franciscan high-grade-metamorphic tectonic blocks. *Bulletin of the Geological Society of America*, *117*(9), 1318–1335. https://doi.org/10.1130/B25593.1

Saleeby, J. B., Harper, G. D., Snoke, A. W., & Sharp, W. D. (1982). Time relations and structural-stratigraphic patterns in ophiolite accretion, west central Klamath Mountains, California. *Journal of Geophysical Research*, *87*(B5), 3831. https://doi.org/10.1029/JB087iB05p03831

Sandmann, S., Nagel, T. J., Froitzheim, N., Ustaszewski, K., & Münker, C. (2015). Late Miocene to Early Pliocene blueschist from Taiwan and its exhumation via forearc extraction. *Terra Nova*, *27*(4), 285–291. https://doi.org/10.1111/ter.12158

Scherer, E. (2001). Calibration of the Lutetium-Hafnium Clock. *Science*, *293*(5530), 683–687. https://doi.org/10.1126/science.1061372

Schweickert, R. A., Armstrong, R. L., & Harakal, J. E. (1980). Lawsonite blueschist in the northern Sierra Nevada, California. *Geology*, *8*(1), 27. https://doi.org/10.1130/0091-7613(1980)8%3C27:LBITNS%3E2.0.CO;2

Shervais, J. W., Choi, S. H., Sharp, W. D., Ross, J., Zoglman-Schuman, M., & Mukasa, S. B. (2011). Serpentinite matrix melange: Implications of mixed provenance for melange formation. *Geological Society of America Special Papers*, *480*(01), 1–30. https://doi.org/10.1130/2011.2480(01)

Shervais, J. W., Kimbrough, D. L., Renne, P., Hanan, B. B., Murchey, B., Snow, C. A., et al. (2004). Multi-stage origin of the Coast Range Ophiolite, California: Implications for the life cycle of supra-subduction zone ophiolites. *International Geology Review*, *46*(4), 289–315. https://doi.org/10.2747/0020-6814.46.4.289

Shervais, J. W., Murchey, B. L., Kimbrough, D. L., Renne, P. R., & Hanan, B. (2005). Radioisotopic and biostratigraphic age relations in the Coast Range Ophiolite, northern California: Implications for the tectonic evolution of the Western Cordillera. *Bulletin of the Geological Society of America*, *117*(5), 633–653. https://doi.org/10.1130/B25443.1

Shyu, J. B. H., Wu, Y.-M., Chang, C.-H., & Huang, H.-H. (2011). Tectonic erosion and the removal of forearc lithosphere during arc-continent collision: Evidence from recent earthquake sequences and tomography results in eastern Taiwan. *Journal of Asian Earth Sciences*, *42*(3), 415–422. https://doi.org/10.1016/j.jseaes.2011.05.015

Sláma, J., Košler, J., Condon, D. J., Crowley, J. L., Gerdes, A., Hanchar, J. M., et al. (2008). Plešovice zircon—A new natural reference material for U–Pb and Hf isotopic microanalysis. *Chemical Geology*, *249*(1–2), 1–35. https://doi.org/10.1016/j.chemgeo.2007.11.005

Snow, C. A., Wakabayashi, J., Ernst, W. G., & Wooden, J. L. (2010). Detrital zircon evidence for progressive underthrusting in Franciscan metagraywackes, west-central California. *Geological Society of America Bulletin*, *122*(1–2), 282–291. https://doi.org/10.1130/B26399.1

Söderlund, U., Patchett, P. J., Vervoort, J. D., & Isachsen, C. E. (2004). The 176Lu decay constant determined by Lu–Hf and U–Pb isotope systematics of Precambrian mafic intrusions. *Earth and Planetary Science Letters*, *219*(3–4), 311–324. https://doi.org/10.1016/S0012-821X(04)00012-3

Stacey, J. S., & Kramers, J. D. (1975). Approximation of terrestrial lead isotope evolution by a two-stage model. *Earth and Planetary Science Letters*, *26*(2), 207–221. https://doi.org/10.1016/0012-821X(75)90088-6

Surpless, K. D., Graham, S. A., Covault, J. A., & Wooden, J. L. (2006). Does the Great Valley group contain Jurassic strata? Reevaluation of the age and early evolution of a classic forearc basin. *Geology*, *34*(1), 21–24. https://doi.org/10.1130/G21940.1

Switzer, G. S. (1945). Eclogite from the California glaucophane schists. *American Journal of Science*, *243*(1), 1–8. https://doi.org/10.2475/ajs.243.1.1

Syracuse, E. M., van Keken, P. E., & Abers, G. A. (2010). The global range of subduction zone thermal models. *Physics of the Earth and Planetary Interiors*, *183*(1–2), 73–90. https://doi.org/10.1016/j.pepi.2010.02.004

Tamblyn, R., Zack, T., Schmitt, A. K., Hand, M., Kelsey, D., Morrissey, L., et al. (2019). Blueschist from the Mariana forearc records long-lived residence of material in the subduction channel. *Earth and Planetary Science Letters*, *519*, 171–181. https://doi.org/10.1016/j.epsl.2019.05.013

Taylor, P., Snow, C. A., & Scherer, H. (2010). Terranes of the Western Sierra Nevada Foothills Metamorphic Belt, California: A critical review terranes of the Western Sierra Nevada Foothills Metamorphic Belt, California: A critical review. *International Geology Review*, *48*(1), 46–62. https://doi.org/10.2747/0020-6814.48.1.46

Tsujimori, T., Matsumoto, K., Wakabayashi, J., & Liou, J. G. (2006). Franciscan eclogite revisited: Reevaluation of the P-T evolution of tectonic blocks from Tiburon Peninsula, California, U.S.A. *Mineralogy and Petrology*, *88*(1–2), 243–267. https://doi.org/10.1007/s00710-006-0157-1

Ukar, E., & Cloos, M. (2019). Cataclastic deformation and metasomatism in the subduction zone of mafic blocks-in-mélange, San Simeon, California. *Lithos*, *346-347*. https://doi.org/10.1016/j.lithos.2019.06.018

Ukar, E., Cloos, M., & Vasconcelos, P. (2012). First ^{40}Ar-^{39}Ar ages from low-T mafic blueschist blocks in a Franciscan Mélange near San Simeon: Implications for initiation of subduction. *The Journal of Geology*, *120*(5), 543–556. https://doi.org/10.1086/666745

van Keken, P. E., Wada, I., Abers, G. A., Hacker, B. R., & Wang, K. (2018). Mafic high-pressure rocks are preferentially exhumed from warm subduction settings. *Geochemistry, Geophysics, Geosystems*, *19*, 2934–2961. https://doi.org/10.1029/2018GC007624

Vermeesch, P. (2012). On the visualisation of detrital age distributions. *Chemical Geology*, *312–313*, 190–194. https://doi.org/10.1016/j.chemgeo.2012.04.021

Wakabayashi, J. (1990). Counterclockwise P-T-t paths from amphibolites, Franciscan Complex, California: Relics from the early stages of subduction zone metamorphism. *The Journal of Geology*, *98*(5), 657–680. https://doi.org/10.1086/629432

Wakabayashi, J. (1999). Distribution of displacement on and evolution of a young transform fault system: The northern San Andreas fault system, California. *Tectonics*, *18*(6), 1245–1274. https://doi.org/10.1029/1999TC900049

Wakabayashi, J. (2011). Mélanges of the Franciscan Complex, California: Diverse structural settings, evidence for sedimentary mixing, and their connection to subduction processes. In *Special publications—Geological Society of America* (Vol. 480, pp. 117–141). Geological Society of America. https://doi.org/10.1130/2011.2480(05)

Wakabayashi, J. (2012). Subducted sedimentary serpentinite mélanges: Record of multiple burial-exhumation cycles and subduction erosion. *Tectonophysics*, *568-569*, 230–247. https://doi.org/10.1016/j.tecto.2011.11.006

Wakabayashi, J. (2015). Anatomy of a subduction complex: Architecture of the Franciscan Complex, California, at multiple length and time scales. *International Geology Review*, *57*(5–8), 669–746. https://doi.org/10.1080/00206814.2014.998728

Wakabayashi, J. (2017a). Sedimentary serpentinite and chaotic units of the lower Great Valley Group forearc basin deposits, California: Updates on distribution and characteristics. *International Geology Review*, *59*(5–6), 599–620. https://doi.org/10.1080/00206814.2016.1219679

Wakabayashi, J. (2017b). Structural context and variation of ocean plate stratigraphy, Franciscan Complex, California: Insight into mélange origins and subduction-accretion processes. *Progress in Earth and Planetary Science*, *4*(1), 18. https://doi.org/10.1186/s40645-017-0132-y

Wakabayashi, J. (2019). Sedimentary compared to tectonically-deformed serpentinites and tectonic serpentinite mélanges at outcrop to petrographic scales: Unambiguous and disputed examples from California. *Gondwana Research*, *74*, 51–67. https://doi.org/10.1016/j.gr.2019.04.005

Wakabayashi, J., & Dumitru, T. A. (2007). ^{40}Ar/^{39}Ar ages from coherent, high-pressure metamorphic rocks of the Franciscan Complex, California: Revisiting the timing of metamorphism of the world's type subduction complex. *International Geology Review*, *49*(10), 873–906. https://doi.org/10.2747/0020-6814.49.10.873

Wakabayashi, J., Ghatak, A., & Basu, A. R. (2010). Suprasubduction-zone ophiolite generation, emplacement, and initiation of subduction: A perspective from geochemistry, metamorphism, geochronology, and regional. *Geology*, *122*(9–10), 1548–1568. https://doi.org/10.1130/B30017.1

Wartho, J.-A., Dodson, M. H., Rex, D. C., & Guise, P. G. (1991). Mechanisms of Ar release from Himalayan metamorphic hornblende. *American Mineralogist*, *76*(1988), 1446–1448.

Wendt, I., & Carl, C. (1991). The statistical distribution of the mean squared weighted deviation. *Chemical Geology: Isotope Geoscience Section*, *86*(4), 275–285. https://doi.org/10.1016/0168-9622(91)90010-T

Wiedenbeck, M., Alle, P., Corfu, F., Griffin, W. L., Meier, M., Oberli, F. V., et al. (1995). Three natural zircon standards for U-Th-Pb, Lu-Hf, trace element and REE analyses. *Geostandards and Geoanalytical Research*, *19*(1), 1–23. https://doi.org/10.1111/j.1751-908X.1995.tb00147.x

Wijbrans, J., & McDougall, I. (1986). ^{40}Ar/^{39}Ar dating of white micas from an Alpine high-pressure metamorphic belt on Naxos (Greece): The resetting of the argon isotopic system. *Contributions to Mineralogy and Petrology*, *93*(2), 187–194. https://doi.org/10.1007/BF00371320

Wijbrans, J., van Wees, J. D., Stephenson, R. A., & Cloetingh, S. A. P. L. (1993). Pressure-temperature-time evolution of the high-pressure, metamorphic complex of Sifnos, Greece. *Geology*, *21*(5), 443. https://doi.org/10.1130/0091-7613(1993)021%3C0443:PTTEOT%3E2.3.CO;2

Wirth, K. R., Bird, J. M., Blythe, A. E., Harding, D. J., & Heizler, M. T. (1993). Age and evolution of Western Brooks Range ophiolites, Alaska: Results from ^{40}Ar/^{39}Ar thermochronometry. *Tectonics*, *12*(2), 410–432. https://doi.org/10.1029/92TC02640